Exploring Near-Field SAR with mmWave Pulsed Coherent Radar

Elina Yrlid

June 19, 2023

Acknowledgements

This thesis was conducted at Acconeer AB in Malmö, Sweden, during the spring of 2023, as the final part of the Electrical Engineering program at the Faculty of Engineering at Lund University (LTH). I would like to give special thanks to Erik Månsson and the team at Acconeer for supporting me during the thesis process and for gladly answering all my questions. Thanks should also go to Maria Sandsten, professor in Mathematical Statistics at LTH, for enthusiastically taking on the role as my supervisor and for always giving useful feedback. I'd also like to acknowledge Daniel Sjöberg, professor in Electrical and Information Technology, for taking the time of introducing me to the concepts of Synthetic Aperture Radar.

Elina Yrlid

Abstract

This thesis explores the option to apply *Synthetic Aperture Radar* (SAR) techniques to image near-field targets utilizing mmWave *pulsed coherent radar* (PCR). The recent development of mmWave radars has broadened the scope for SAR, but there are few concrete examples explaining and demonstrating the fundamental SAR algorithms from a PCR perspective.

This thesis aims to address this gap by investigating the imaging capabilities of near-field SAR, where the curvature of the incoming waves has to be considered. The focus is on a comparative analysis of two distinct imaging approaches: frequency-based image formation and time-based image formation. The two approaches are compared using elementary algorithms in each category: *Doppler Beam Sharpening* and *Global Backprojection*. The comparison involves explaining the theory and approximations of each algorithm, discussing the shortcomings, and examining the expected effects when applying them in near-field applications. These effects are later exemplified through simulations. Finally, the algorithms are applied to measurements made using the Acconeer A121 PCR system, showcasing the remarkable potential of basic SAR techniques in rendering intricate images of near-field targets. By making these investigations, we endeavor to contribute to the academic understanding and practical utilization of near-field SAR with PCR systems.

Contents

List of Abbreviations

ADC - Analog-to-digital converter

DBS - Doppler Beam Sharpening

EM - Electromagnetic

FFT - Fast Fourier Transform

FMCW - Frequency Modulated Continuous Wave

FWHM - Full Width at Half Maximum

MUR - Maximum Unambiguous Range

PCR - Pulsed Coherent Radar

PRI - Pulse Repetition Interval

PRF - Pulse Repetition Frequency

RDA - Range Doppler Algorithm

RMA - Range Migration Algorithm

SAR - Synthetic Aperture Radar

SNR - Signal-to-noise ratio

Chapter 1

Introduction

Radar is a technology based on transmitting and receiving electromagnetic waves to determine the distance to a target. For a single-channel system, with only one transmit and one receive antenna, this information is one-dimensional in space [1]. This means that the distance to a target can be determined, but not the angle or direction to the target. However, by moving the system and measuring from different positions in space, an additional dimension of information is introduced. By exploiting the correlation between the measured points at different antenna positions, one can create an image with better spatial resolution than could be achieved from a stationary system. This is the fundamental concept of *Synthetic Aperture Radar* (SAR) [2]. Moving the radar system is equivalent to mimicking a larger antenna, thus creating a synthetic aperture. This method was originally developed for imaging distant targets using air or spacecraft [3], but with the development of mmWave radars, the scope for SAR has broadened, and many near-field applications have been presented in recent years.

The focus of this thesis is to explain and demonstrate the theory on which SAR is based, while applying a *pulsed coherent radar* (PCR) perspective. Many articles and texts regarding SAR describe it in a strict frequency context, which correlates well when using frequency-modulated radars [4]. However, when using pulsed radar without frequency modulation, where the outputted data is already converted to range, the strict frequency context becomes overly complicated. The aim is to bridge the gap between these two viewpoints and simultaneously introduce the reader to the concepts of SAR, starting with the theory and concluding with near-field SAR images generated from measured data.

The first part of the thesis provides an overview of radar principles and SAR, describing the resolutions, sampling requirements, and commonly used approximations. The two main categories for image formation are also introduced: frequency-based image formation and time-based image formation. In the next chapter two algorithms, one from each category, are described in greater detail. The purpose is to show the differences between the two approaches and explain the limitations of each method, to provide an

understanding of when each method is suitable to apply. The following chapter includes simulations to connect the previously presented theory with its effect on imaging. The data is also generated with varying degrees of noise and errors to illustrate how these uncertainties manifest themselves in the resulting images. Chapter 5 applies the same algorithms to collected sensor data to demonstrate the possibilities of near-field SAR. The two approaches are compared and evaluated in different scenarios. The thesis concludes with a summary and discussion of the previous chapters.

The thesis can be described as an introduction to SAR using PCR with objective to:

1. Provide a fundamental description of SAR using a PCR perspective.
2. Exemplify the possibilities of near-field SAR and demonstrate how images can be created with relatively simple algorithms.
3. Demonstrate the different advantages and disadvantages between frequency- and time-based algorithms and provide an understanding of when it is appropriate to apply each method.
4. Give an intuitive understanding of how noise and errors affect the final images.

Chapter 2

Overview

2.1 Radar - Basic Principles

The word radar was originally an acronym for *radio detection and ranging*. Today, the word describes a whole field of technology where radiofrequency electromagnetic (EM) waves are transmitted towards a region of interest. The fundamental idea of radar is that these waves are reflected by objects in the region to later be received by the radar system [2]. The distance to the objects is determined by the time between the transmitted signal, the received signal, and the propagation speed as

$$R = \frac{c\Delta T}{2} \tag{2.1}$$

where R is the distance to the target, c is the speed of light, which coincides with the propagation speed of an EM wave, and ΔT is the time between the transmitted and received signals. The right-hand side of the equation is divided by two since the wave propagates first towards and then away from the target, with the assumption that the transceiver and receiver antenna is the same or that the distance between them are negligible [5].

Radar was primarily developed for military purposes to detect objects and image regions many kilometers away and is still today mainly used in far-range situations, for instance, air and space-born scenarios. The majority of radar systems, therefore, operate on frequencies between 300 MHz and 35 GHz, which corresponds to wavelengths between 1 m and 8.6 mm [5]. These longer wavelengths are usually utilized in far range applications since less of the signal energy is dissipated during the travel compared to short wavelengths. However, short wavelengths have the ability resolve smaller features [1]. In recent years there has been immense development within the mmWave radar segment, which usually operates at even higher frequencies. This has broadened the use of commercial radar to fields such as automation, automotive, and IoT products.

2.2 Pulsed Coherent Radar

There exist many different types of radar systems. However, the applied radar waveforms can be divided into two main categories: *continuous wave radar* and *pulsed radar*. As the name suggests, the continuous wave (CW) waveform consists of a continuously transmitted signal, where the receiver operates in parallel with the transmitter. One way to determine the signal's round-trip time, is to change the frequency of the transmitted wave during transmission to create time markers in the signal [2]. By measuring the frequency of the received signal, the range can be determined. This method is called *frequency modulation* (FM), and radar systems that apply this technique are typically called FMCW-radar, which stands for *frequency modulated continuous wave*. [5]

Pulsed radar, on the other hand, makes use of short transmitted pulses, where the distance to the object is determined by the time it takes for the pulse to return to the sensor. A pulse consists of a carrier wave that is transmitted under a short period of time [5]. Ideally, the pulse has the shape of a square wave, but in reality this is rarely the case. The shape is instead often compared to a Gaussian function (see figure 2.1). The shape of the signal is referred to as the envelope.

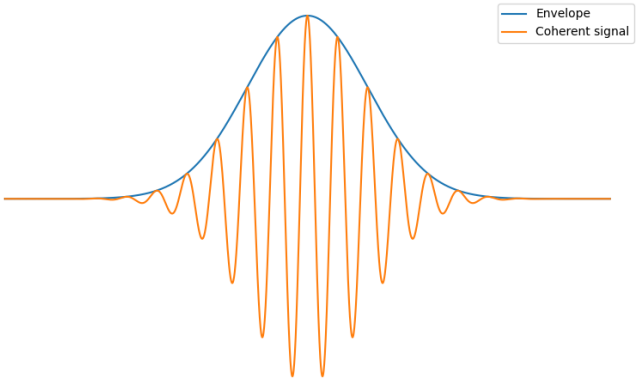

Figure 2.1: The figure illustrates a generic wavelet, where the orange graph is the coherent signal and the blue graph shows the shape of the signal called the envelope.

The term *coherent* means that the returned signal contains both amplitude and phase information, which is useful in many applications [1]. The phase information can, for example, be utilized to detect very small (less than half a wavelength) movements.

The radar system used in this thesis is the Acconeer A121 sensor, which is a pulsed coherent radar. The concepts and theories discussed and explained will be based on this system. The emitted pulses have a carrier frequency of 60.5 GHz, which corresponds to an approximate wavelength λ of 5 mm [6]. To measure over an appointed range interval, the A121 utilizes a set of pulses referred to as a *sweep*. The time between each pulse is called the *pulse repetition interval* (PRI), which is inversely proportional to the *pulse repetition frequency* (PRF) [7],

$$\text{PRF} = \frac{1}{\text{PRI}} \, . \tag{2.2}$$

The PRF limits the *maximum unambiguous range* (MUR) for the sensor since the transmitted pulse must be reflected by an object and received by the receiver, before the next pulse is transmitted, for the range to be unambiguously determined. The MUR is given by the following expression, assuming the pulse length is short in relation to the PRI,

$$\text{MUR} = \frac{c}{2 \cdot \text{PRF}} \tag{2.3}$$

where c is the speed of light [8].

An *analog-to-digital converter* (ADC) is used to sample the receiver at discrete time intervals to reconstruct the echo from the transmitted pulses. During a sweep using an Acconeer system, each transmitted pulse will be dedicated to a specific distance. The sensor transmits a pulse, and at the time at which the pulse should have been returned from that distance, the receiver is sampled. The reason why the receiver is not continuously sampled is because of the high bandwidth of the signal. During a sweep, the receiver is sampled with an increased delay in between each sample to correspond to longer and longer distances. The smallest measurable distance step is approximately 2.5 mm. Thus, for a range interval between 0.1-0.2 m, one could obtain 41 data points per sweep, one point per 2.5 mm.

More detailed information about the system can be found in section 5.1.

2.3 Synthetic Aperture Radar

This following section will outline the concepts of *Synthetic Aperture Radar* (SAR).

2.3.1 Background

SAR is a method for creating images from radar data. The method is widely used with airborne or satellite-borne radar systems to create high-resolution maps of remote targets. The concept was developed during the 1950s, and further research was widely funded by the U.S. military and NASA [3]. Compared to optical images, radar images have the advantage of being able to be captured at night and in bad weather conditions. It is also possible to achieve fine resolution at very large ranges [2]. These are some of the reasons why the method grew popular for military applications. There has been a lot of progress in SAR research since the 1950s, and with the development of mmWave radars, new applications for SAR have been introduced, such as concealed weapons detection [9, 10] and non-invasive medical imaging [11].

The concept of SAR is based on the understanding that the radar beam width determines the spatial resolution of the data. The narrower the beam width, the higher the resolution. The resolution for an antenna can be approximated as

$$\Delta x = R\frac{\lambda}{D} \tag{2.4}$$

where Δx is the resolution (in unit distance) at range R, λ is the wavelength, and D is the aperture size (in this case, the antenna length). The factor $\frac{\lambda}{D}$ is the approximation of the beam width in radians. [5]

For a short antenna, the beam width is wide and the resolution is coarse. To achieve a finer resolution, a larger antenna is needed, which is not feasible due to the resulting large radar system. Instead, a synthetic aperture can be created by moving the existing antenna along a path and collecting data at certain intervals. This mimics a larger antenna and results in a finer spatial resolution, which is the fundamental idea of SAR.

There are two commonly used collection modes for SAR: *stripmap SAR* and *spotlight SAR* [5]. In stripmap SAR the platform (on which the radar is located) moves a long a straight-line path. The antenna beam is off to one side and is perpendicular to the collection path. The area illuminated by the radar beam is shifted for each new position along the path (see Figure 2.2a). In spotlight SAR the radar is always pointed towards the scene of interest and the same scene is instead illuminated from different angles. This can be achieved by either turning the radar as in Figure 2.2b or by having a circular collection path as in Figure 2.2c. This thesis will, however, focus on the stripmap mode and the calculations will be based on the corresponding geometry.

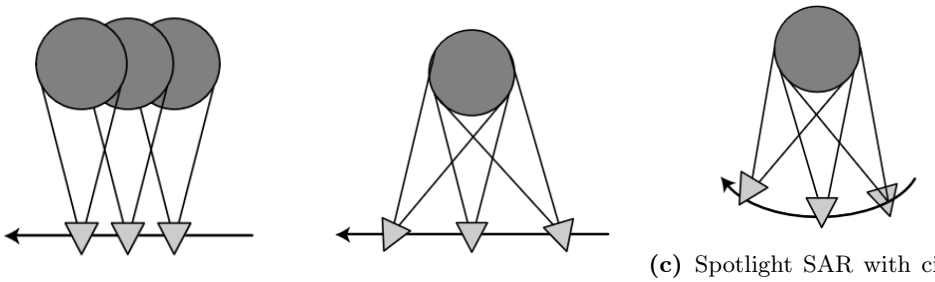

(a) Stripmap SAR **(b)** Spotlight SAR **(c)** Spotlight SAR with circular path

Figure 2.2: Illustrates different collective modes for SAR. (Image source: [5])

A general stripmap SAR example can be seen in Figure 2.3. The figure shows the common terms used when describing SAR and the resulting image. In most SAR applications the antenna beam will be pointed of to the side of the platform. This differs from optical images, which are usually captured directly above the scene of interest. The reason for this is to avoid ambiguities in the resulting SAR image. Since each sweep only contains phase and amplitude information for each range-point, there is no angular information

to determine the direction of the scatterer's location. If the beam was pointed straight down from the platform, it would be impossible to know if the received echoes originated from the left or right side of the track. By looking at the scene from an angle, one can assume that the data at shorter ranges corresponds to the area of the scene that is closest to the sensor, and the data at further ranges correspond to the area further away in the scene.

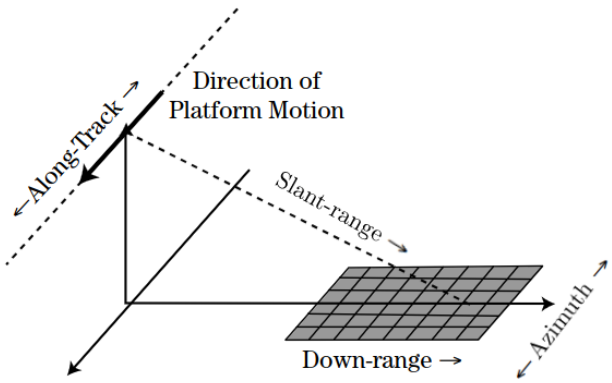

Figure 2.3: Illustrates the most commonly used terms when speaking of SAR geometry. SAR images are usually defined as a function of along-track and slant-range coordinates, or down-range and azimuth coordinates. (Image source: [5])

2.3.2 Near- and far-field

In radar and other electromagnetic applications, two terms that are commonly used are *near-field* and *far-field*. The far-field is a region located far enough from the sensor that the waveform curvature of the returning pulses can be approximated as planar. This approximation is called the *far-field approximation* and is in turn based on the *Fraunhofer approximation* or *Fraunhofer region*. The region is defined as

$$R_f = \frac{\pi}{4}\frac{D^2}{\phi\lambda} \tag{2.5}$$

where R_f is the distance at which the Fraunhofer region starts, D is the maximum aperture, ϕ is the maximum allowed phase error and λ is the wavelength [12]. The far-field is defined as the Fraunhofer region with $\phi = \pi/8$ [5]

$$R_{f,\text{far-field}} = \frac{2D^2}{\lambda}\,. \tag{2.6}$$

In other words, if the waveform curvature is less than $\lambda/16$ over a given aperture, it is considered planar. This condition is somewhat arbitrarily decided but universally accepted.

For many SAR applications, it is important to know whether the targets are located in the near-field or far-field since this affects which algorithms are suitable to apply. In the far-field, range migration is assumed to be negligible, while in near-field applications, range migration has to be considered, or it will affect the generated images. The term *range migration* refers to the phenomenon where the echo from a single scatterer is spread over several range bins because of the incoming wave's curvature [5]. The concept is described in more detail in section 3.1.2.

2.3.3 Theoretical resolutions and sampling requirements

A common way to describe the physical limits of a SAR image is by the term *resolution*. There are different kinds of resolution but when referring to SAR images one often refers to *spatial resolution* which is expressed in units of distance. The resolution is defined as the limit of the ability to resolve two closely spaced scatterers. A common way to describe if two scatters can be resolved separately is if the distance between the main peaks are larger or equal to the *full width at half maximum* (FWHM) of the peaks (see Figure 2.4) [13]. The corresponding term when speaking of frequency is the *half-power bandwidth*.

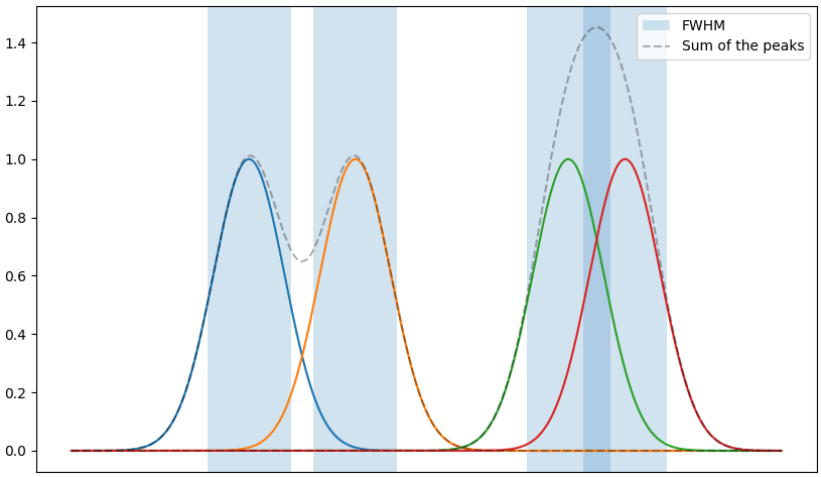

Figure 2.4: The figure illustrates the concept of resolution. The blue and orange curve can be resolved from each other since the distance between them is greater than the FWHM. The green and red curve cannot be resolved since the distance between is shorter than the FWHM.

For SAR images there are two main resolutions that limits the image quality: range resolution and azimuth resolution. The resolution for any imaging system using two-way propagation is given by

$$\Delta = \frac{c}{2B} \tag{2.7}$$

where c is the speed of the propagation medium and B is the half-power bandwidth of

the signal in the direction in which the resolution is desired to be determined [2].

Range Resolution

For the range resolution, the bandwidth would be equivalent to the bandwidth of the frequency-transformed envelope of the transmitted signal. However, since the data from the employed PCR system already corresponds to distances, the resolution is the same as the FWHM of the envelope. This reasonable since an infinitely short envelope corresponds to an infinite bandwidth, which in turn results in an infinitely fine resolution.

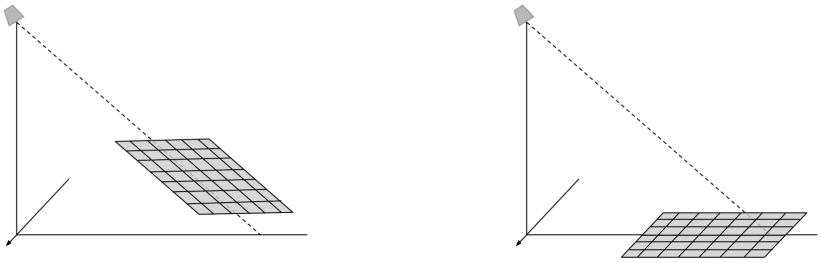

(a) Image in slant range **(b)** Image in down range

Figure 2.5: Illustrates different kinds of collective modes for SAR. (Image source: [5])

Furthermore, there are many SAR applications where the desired image is not placed in the slant-range plane but rather in the down-range plane, such as mapping a flat area. Figure 2.5 shows the difference between an image placed in slant range and down range respectively. The down-range resolution can be expressed as a function of the sensor's look angle from the ground, the range resolution and the slant of the image plane,

$$\Delta\text{down-range} = \frac{\Delta\text{range}}{\sin(\theta_l - \theta_s)} \tag{2.8}$$

where θ_l is the look-angle and θ_s is the slant angle of the image plane (see Figure 2.6). The best possible down-range resolution is the range resolution which is achieved when the down-range axis is equal to the slant-range axis.

Azimuth Resolution

The azimuth resolution for a SAR system is usually expressed as some version of the following expression,

$$\Delta\text{azimuth} = \frac{\lambda_c}{2\theta_{3\text{dB}}} \tag{2.9}$$

where λ_c is the carrier wavelength and $\theta_{3\text{dB}}$ is the half-power beam width of the radar sensor [5]. However, the above resolution expression includes a number of approximations which are difficult to detect at first glance.

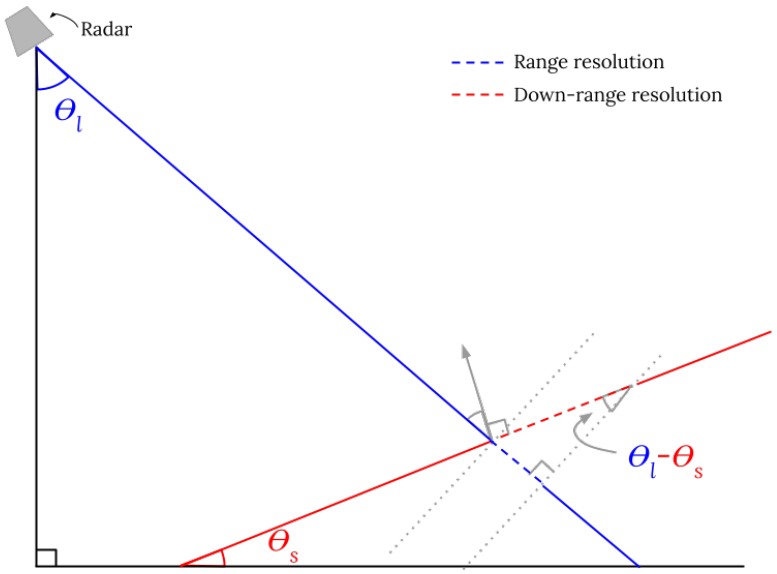

Figure 2.6: The figure shows how the down-range resolution depends on the look-angle θ_l, the slant of the image plane θ_s and the range resolution. The blue line is the direction of the radar beam and the red line is the image plane.

To derive the azimuth resolution, Δazimuth, there are three main parts that needs to be understood:

1. The half-power beam width of the sensor, $\theta_{3\text{dB}}$, gives the aperture length, D_{SAR}.
2. The aperture length, D_{SAR}, gives the half-power beam width for the synthetic aperture, θ_{SAR}.
3. The half-power beam width, θ_{SAR}, gives the azimuth resolution for the SAR system.

Firstly, the aperture length, D_{SAR}, is given by the maximum distance the radar can move along the collection path while still keeping the same scatterer inside its beam footprint (see Figure 2.7). The aperture length can therefore be expressed as a function of the half-power beam width $\theta_{3\text{dB}}$,

$$D_{SAR} = 2r \cdot \tan\left(\frac{\theta_{3\text{dB}}}{2}\right) \tag{2.10}$$

where r is the range to the center of the scene. If $\theta_{3\text{dB}}$ is small, then D_{SAR} can be approximated as $D_{SAR} \approx r \cdot \theta_{3\text{dB}}$.

The second part of the derivation is to understand how the aperture length, D_{SAR}, affects the synthesized antenna's beam width, θ_{SAR}. The half-power beam width, $\theta_{3\text{dB}}$, for any aperture (real or synthesized) is universally approximated as

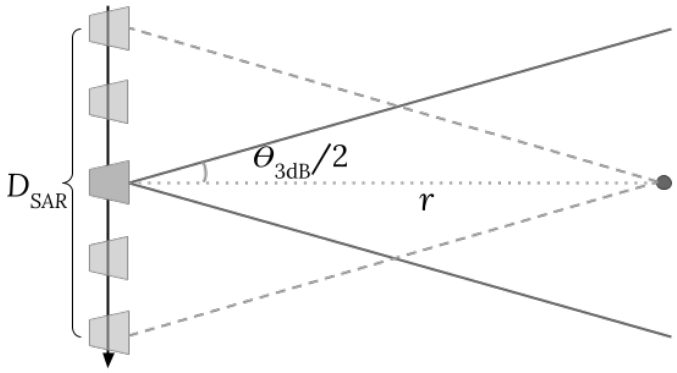

Figure 2.7: The figure illustrates that the beam footprint is equal to the aperture length D_{SAR}, and that the aperture length can be expressed as a function of the range r and the half-power beam width $\theta_{3\text{dB}}$.

$$\theta_{3\text{dB}} \approx \frac{\lambda}{D} \tag{2.11}$$

where λ is the wavelength and D is the length of the aperture [14].

However, for a SAR-system where the transmit location is moved every sample, instead of the whole aperture being used in transmission like for real antennas, a factor $\frac{1}{2}$ is added to the beam width,

$$\theta_{SAR} \approx \frac{\lambda_c}{2D_{SAR}} \tag{2.12}$$

where λ_c is the carrier wavelength and D_{SAR} is the length of the SAR aperture [5].

Thirdly, two scatterers can be resolved only if they are located in two different beam footprints of the synthetic aperture. Therefore, the SAR azimuth resolution is equal to the synthetic antenna's beam footprint. This footprint can be calculated in a similar manner as D_{SAR} in Equation 2.10,

$$\Delta\text{azimuth} = 2r \cdot \tan\left(\frac{\theta_{SAR}}{2}\right) \tag{2.13}$$

this expression can also be approximated when θ_{SAR} is small, as $\Delta\text{azimuth} \approx r \cdot \theta_{SAR}$.

If the equation in 2.13 is combined with Equations 2.12 and 2.10, the following expression is obtained,

$$\Delta\text{azimuth} = 2r \cdot \tan\left(\frac{\lambda_c}{4 \cdot D_{SAR}}\right) = 2r \cdot \tan\left(\frac{\lambda_c}{4 \cdot 2r \cdot \tan\left(\frac{\theta_{3\text{dB}}}{2}\right)}\right) \ . \tag{2.14}$$

Assuming both $\theta_{3\text{dB}}$ and θ_{SAR} are small the equation can be simplified as

$$\Delta\text{azimuth} \approx \frac{\lambda_c}{2\theta_{3\text{dB}}} \tag{2.15}$$

which is the same expression that was presented in the beginning of the section. Note that this expression does not depend on the range r, which implies that the azimuth resolution is independent of the range. This is reasonable since at longer ranges the aperture becomes longer which increases the resolution the same amount as the range decreases it. The expression also shows that a wider half-power beam width for the radar sensor actually results in finer resolution for the synthetic aperture. This might seem contradictory at first, but since a wide radar footprint results in a large aperture, the final azimuth resolution becomes finer.

Sampling Requirements

In order to uphold the theoretical azimuth resolution, the sample spacing along the collection path needs to be sufficiently small. The sampling requirement is based upon the Nyquist criterion, which declares that a signal must be sampled at least every half wavelength in order to avoid aliasing.

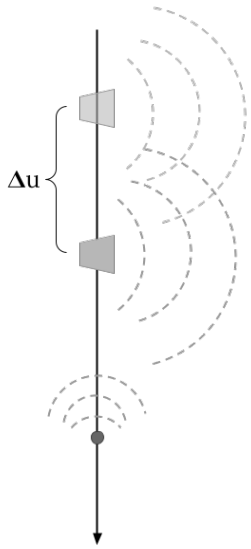

Figure 2.8: Shows a radar sensor with a beam width of 180 degrees that is moved along a collection path. The circle on the path represents a single point scatterer. The distance a long the collection path between each sample/sweep is marked as Δu.

Imagine a radar with a half-power beam width of 180 degrees that is moved along a straight collection path. A single scatterer is located on the collection path (see Figure 2.8). The difference in the signals' traveled distance to the scatterer, between two

sampling positions, cannot exceed $\lambda/2$. This condition can be expressed as

$$\Delta R = 2 \cdot \Delta u \leq \frac{\lambda}{2} \tag{2.16}$$

where Δu is the distance between the two radar sampling positions along the path. The distance is multiplied by 2 because of the two-way propagation. This gives the following sampling requirement for u,

$$\Delta u \leq \frac{\lambda}{4} \, . \tag{2.17}$$

However, most radar systems have a smaller half-power beam width than 180 degrees and can thus sample more sparsely. Assuming the far-field approximation and a single scatterer located at the trailing edge of the beam (see Figure 2.9), the range between two sample points is given by

$$\Delta R = 2 \cdot \Delta u \cdot \sin\left(\frac{\theta_{3\text{dB}}}{2}\right) \leq \frac{\lambda}{2}, \quad R \gg \Delta u \tag{2.18}$$

where $\theta_{3\text{dB}}$ is the half-power beam width. This gives the sampling requirement for the far-field:

$$\Delta u \leq \frac{\lambda}{4 \sin\left(\frac{\theta_{3\text{dB}}}{2}\right)}, \quad R \gg \Delta u \, . \tag{2.19}$$

2.3.4 3D Image Formation

In the above sections, all cases have assumed a one-dimensional aperture with information spread in both azimuth and range, allowing the generation of a 2D SAR image. However, if a two-dimensional aperture is used, an additional information dimension is introduced, referred to as *elevation*. A two-dimensional aperture can have various configurations, with the simplest being two separate one-dimensional apertures separated by some distance and illuminating the same target with slightly different observation angles. The resulting 2D SAR images will have different phases, indicating the location of each pixel in three-dimensional space. By utilizing this information, 3D SAR images can be generated, similar to how SAR topology maps are created. The resolution in the elevation dimension will depend on the shape and size of the 2D aperture, just as the azimuth and down-range resolutions discussed in section 2.3.3.

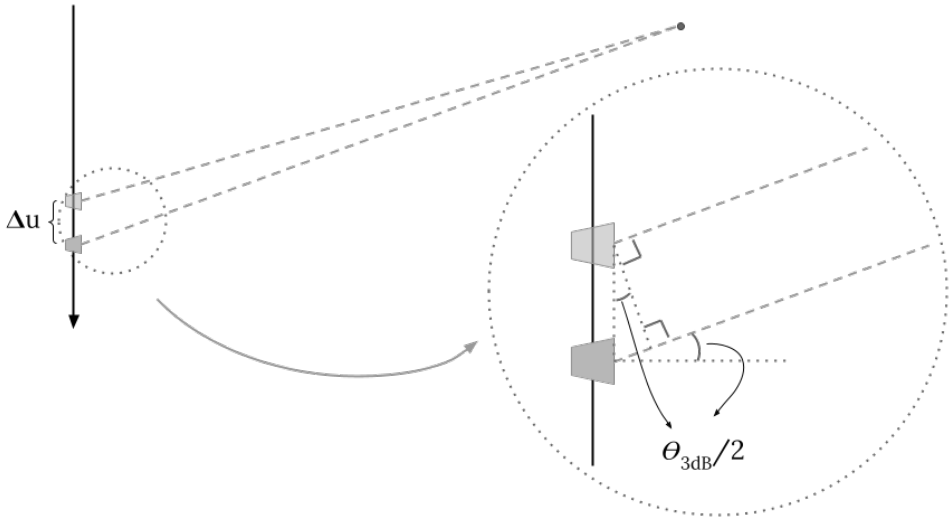

Figure 2.9: Illustrates the range difference to a scatterer between two sample positions, assuming the scatterer is located in the far-field.

2.3.5 Image Formation Algorithms

The basic concept and idea of SAR has been described in the previous sections, however, the process of generating the images has yet to be explained. There are countless numbers of SAR image formation algorithms that have been developed, all with different advantages and drawbacks. These algorithms can be divided into two main categories: frequency domain-based algorithms and time domain-based algorithms. This thesis will focus on two algorithms that can be seen as the extremes in each category: *Doppler Beam Sharpening* (frequency-based) and *Global Backprojection* (time-based). The reason for focusing on these two algorithms is that they together form the basis on which all other SAR algorithms are developed. Many of the other algorithms developed after these two focus on reducing the impact of the disadvantages of the methods.

The main advantage of Doppler Beam Sharpening is that it is very computationally efficient. However, it does not account for range migration or phase orders above linear, meaning it assumes the target is in the far-field. Additionally, it requires uniform sampling since it applies the FFT, and the image size and position are restricted by the aperture. On the other hand, the main advantages of Global Backprojection are that it works in both near-field and far-field, the image position and size can be freely selected, and the aperture does not have to be uniformly sampled. The downside is that the algorithm is extremely computationally intensive, making it impossible to use in any real-time imaging scenarios.

Two other commonly used frequency-based algorithms are the *Range Doppler Algorithm* [15] and the *Range Migration Algorithm* [16], often referred to as RDA and RMA respectively. Both of them address the range migration problem with Doppler Beam

Sharpening. However, RDA only focuses the image at one range, making it applicable only for targets far away, whereas RMA corrects for the range migration for all ranges, making it popular in near-field applications. There have also been a couple of algorithms developed to tackle the computational complexity of Global Backprojection. Two of the more famous algorithms are the fast-backprojection [17] and the fast-factorized backprojection [18]. The best choice of algorithm, however, depends entirely on the application and the requirements on memory, computational complexity, and image quality.

Chapter 3

Theory and Method

This section will provide a more detailed description of the two algorithms used for the simulations and measurements in this thesis: Doppler Beam Sharpening and Global Backprojection. It will also introduce and explain the two image quality factors used to evaluate the generated images in the following chapters.

3.1 Algorithms

Many SAR algorithms, including the two presented in this thesis, assume that the image formation calculations can be divided into two main steps: range compression and azimuth compression. However, this assumption is based on an approximation called the *stop-and-hop approximation* [19]. This approximation assumes that the sweep duration, during which pulses for a given range interval are transmitted, is short enough so that the platform movement during the transmission is insignificant and can be deemed stationary during the sweep.

Considering a stationary, isotropic scatterer located in three-dimensional space, the generic received signal from a pulsed radar system moved along a path can be expressed as

$$s_n(t) = A_n \cdot W(t - t_n) \exp\{j2\pi f_c(t - t_n) + j\phi_0\} + \eta \tag{3.1}$$

where $\mathbf{s_n} = [s_n(t_{d_1}), ..., s_n(t_{d_i})]$ is a vector of data points for a given range interval (sweep), and t is the time corresponding to the different ranges d, in the sweep (in some literature referred to as fast-time). The round-trip time between the transmitter, scatterer, and receiver is t_n, where n is the position index, i.e. the data index for new antenna positions along the collection path. The amplitude adjustment factor A_n depends on the radar cross-section of the scatterer, antenna gains, etc. It also includes the propagation loss given by the distances from the transmit-antenna to the scatterer and the distance from

the scatterer to the receiver-antenna. $W(t)$ is the envelope of the signal, f_c is the carrier frequency, ϕ_0 is the initial phase, and η is additive noise. An important observation to be made from the expression above is that without the *stop-and-hop approximation*, t_n implicitly becomes a function of time t caused by movement during sweep transmission.

For any SAR signal, the energy of the signal is spread in both range and azimuth. It is desirable to focus the energy as narrowly as possible, which is done by a process called *compression*. Compression is applied to shorten the duration of the received signal. It is usually performed using a matched filter since it maximizes SNR in the presence of additive noise [19]. The idea is that the matched filter should be as similar to the transmitted signal as possible, where the resulting output after compression is a correlation between the transmitted and received signal. In the case where position indexed time t_n is implicitly dependent on time t, the compression needs to be done by a two-dimensional matched filter, which is computationally heavy. By applying the *stop-and-hop approximation*, t and t_n become independent of each other, and the compression can instead be done in two one-dimensional steps, one in range and one in position index (azimuth). This also allows us to optimize each step individually.

The exact method used for range compression is dependent on the specific radar system. However, a range-compressed signal should be expressed as a function of space, which usually implies as a function of range or wavenumber (radians per unit distance). Since the range-compressed signal is discretely sampled by the ADC at time points which corresponds to specific ranges, the resulting signal can be expressed as a discrete version of equation 3.1,

$$R_n(d) = A_n \cdot W(d) \exp\{j2\pi f_c d + j\phi_0\} + \eta \tag{3.2}$$

where $R_n(d)$ is the range-compressed signal received at index n at the discrete range (or distance) d.

The azimuth compression depends on the image formation algorithm, and there are many different algorithms to choose from. The choice of algorithm is commonly impacted by the desired image quality, computation and memory requirements, distance to the scatterer, and the properties of the data collection path. In the following sections, two different ways of performing azimuth compression will be described.

3.1.1 Global Backprojection

Global Backprojection, which can also be referred to as time-domain backprojection, is the most straightforward matched filtering approach in the time domain. In this thesis, it will be referred to as simply *backprojection* for the sake of notation. The process coherently integrates the received signal over each position along the collection path to form the image. The complex image value I, located in a 2-dimensional space at the pixel location p, is given by [20]

$$I(p) = \sum_n R_n(d(n,p)) \exp\{j2\frac{2\pi f_c}{c} d(n,p)\} = \sum_n R_n(d(n,p)) \exp\{j2k_c d(n,p)\}, \quad (3.3)$$

where $d(n,p)$ is the distance between the pixel p and the sensor position at index n (see Figure 3.1). $R_n(d(n,p))$ is the range-compressed signal received at index n, interpolated to the distance $d(n,p)$. k_c is the carrier wavenumber, which is equal to $\frac{2\pi f_c}{c}$.

Note that the expected phase of $R_n(d(n,p))$ is $\exp\{-j2k_c d(n,p)\}$. When multiplying $R_n(d(n,p))$ with the complex conjugate of its expected phase, the result is a correlation between the actual phase and the expected one. The correlation term summed over all instances n gives a matched filter, which results in azimuth compression.

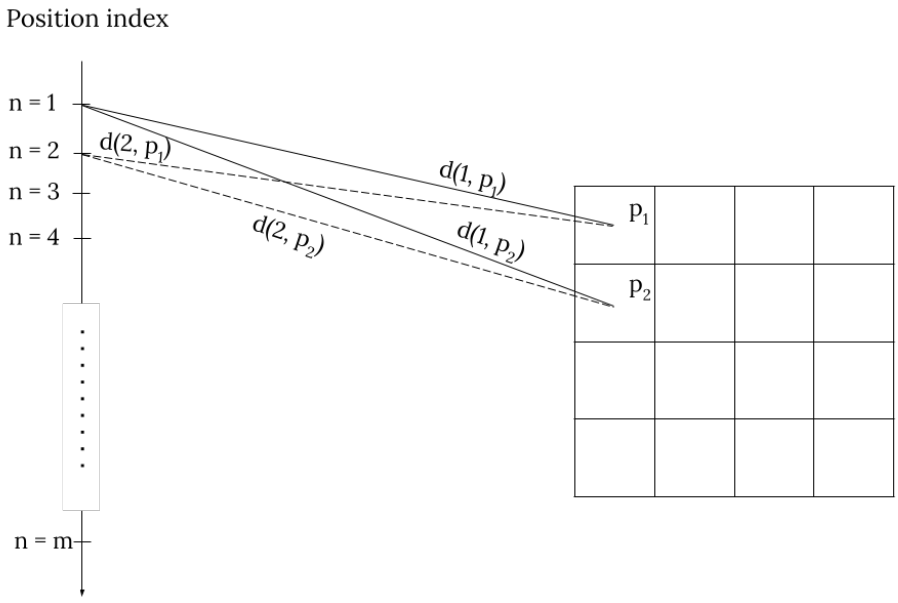

Figure 3.1: The figure illustrates how the distance $d(n,p)$ depends on each position index n and pixel p. For each position index n, $d(n,p)$ will have the same shape as the resulting image which is equal to the number of pixels. This is the reason why global backprojection is so computationally demanding.

The computational complexity for an image with $n \times n$ pixels using m aperture positions is proportional to $O(n^2 \cdot m)$ [17]. The same algorithm can be used to attain a three-dimensional image by placing the pixel p in a three-dimensional space. However, the computational complexity will scale with this change, and for an image with $n \times n \times n$ pixels and m aperture positions, the complexity is given by $O(n^3 \cdot m)$.

3.1.2 Doppler Beam Sharpening

Doppler Beam Sharpening (DBS) is the simplest approach to azimuth compression in the frequency domain. It involves applying a Fourier transform over each range bin in range-compressed data, under the assumption that the targets are far enough away so that the echo from a target is contained within a single range bin. The following paragraphs will describe in more detail how this works. These basic concepts create the basis for many SAR algorithms that have been developed to overcome the shortcomings of DBS while still taking advantage of the computationally efficient calculations that can be made in the frequency domain.

Radar Echoes

To begin the derivation of why DBS can be used for azimuth compression under certain conditions, one has to start with the radar echoes collected from a single point scatterer.

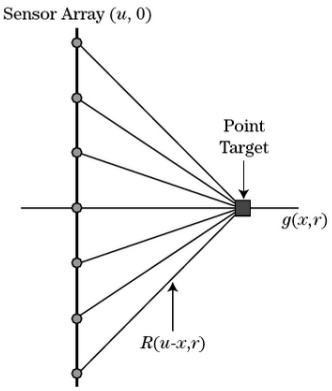

Figure 3.2: The figure shows a point scatterer located at azimuth position x and range position r. A sensor is moved along a linear path creating a sensor array at positions (u, r), $r = 0$. (Image source: [5])

Figure 3.2 illustrates a point scatterer captured by a sensor at several positions along a linear track. The range to the target can be expressed using the Pythagorean theorem as

$$R_n(u - x, r) = \sqrt{(u - x)^2 + r^2} \tag{3.4}$$

where u is the azimuth position of the sensor and n is the position index. x is the azimuth position of the target and r is the slant-range to the target when $u = 0$. The resulting radar echo from this track can be seen in Figure 3.3. The figure illustrates that the sweeps made at the edges of the aperture will register the object in range bins further away compared to the sweeps made at $u = 0$, which makes sense since the distance to the target is greater at these positions. This phenomenon, where the echo from a scatterer is spread over several range bins, is called *range migration*.

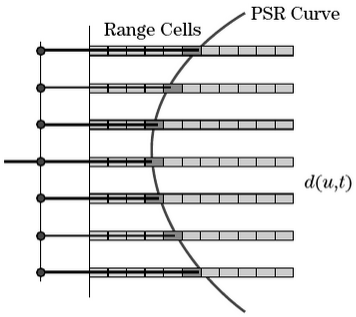

Figure 3.3: The figure shows the resulting radar echo/point spread response (PSR) for each sensor position when looking at the point scatterer in Figure 3.2. (Image source: [5])

Assumptions

When DBS is used, one assumes that the targets are sufficiently far away and that the aperture is short enough to approximate each echo as a planar wave (see Figure 3.4). Under this approximation, the echoes can be described as a one-dimensional function confined to a single range bin.

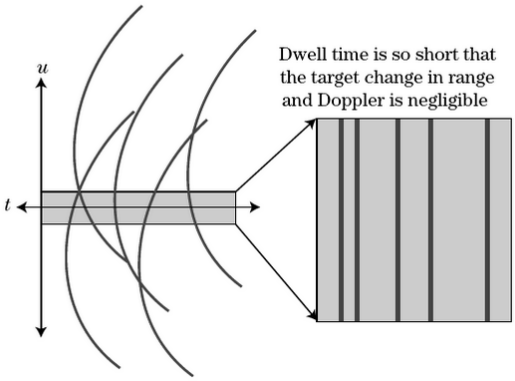

Figure 3.4: The figure illustrates the plane wave approximation required for DBS. The method assumes that the scatterers are far away and that the collection path (dwell time) is short enough so that the received echoes can be perceived as planar. (Image source: [5])

The time function t for each echo can be written as

$$t(u;x,r) = \frac{2}{c}\sqrt{(u-x)^2+r^2} = \frac{2}{c}r\sqrt{1+\frac{(u-x)^2}{r^2}}\ . \tag{3.5}$$

To simplify future derivations the square root is removed by performing a binomial expansion given by

$$(1+w)^q \approx 1 + qw,\ w \ll 1\ . \tag{3.6}$$

By using Equation 3.5 together with Equation 3.6 with $q = \frac{1}{2}$ the time t can now be written as

$$t(u;x,r) \approx \frac{2}{c} r \left(1 + \frac{(u-x)^2}{r^2}\right) = \frac{2}{c}\left(r + \frac{u^2}{2r} - \frac{ux}{r} + \frac{x^2}{2r}\right),\ (u-x) \ll r\ . \tag{3.7}$$

Since the assumption shown in Figure 3.4 was that the distance to the target was much larger than the aperture, the condition $(u-x) \ll r$ is satisfied. Equation 3.7 now describes an approximation of the hyperbolic radar echo. Since each echo is confined to a single range bin the only way to tell where in azimuth the scatterer is located is to consider the change in phase between each sensor position along the track. This phase change can be expressed as a difference in time,

$$\Delta t(u;x,r) \approx \frac{2}{c}\left(\frac{u^2}{2r} - \frac{ux}{r}\right)\ . \tag{3.8}$$

Rewriting this expression from time difference to phase difference in radians,

$$\Delta\psi = 2\pi f_c \Delta t(u;x,r) \approx 2k_c\left(\frac{u^2}{2r} - \frac{ux}{r}\right)\ . \tag{3.9}$$

Note that the first term does not depend on the scatterer position x and serves only to modulate the data by a quadratic phase function. In the most basic form of DBS this term is ignored as long as the error introduced by removing it only causes a negligible effect on the resulting phase, this limit is often set to $\frac{\pi}{2}$. For an aperture of length D_{SAR} with the middle being located at $u = 0$, the maximum value for the quadratic phase term is at the edges of the aperture at $\pm D_{SAR}/2$,

$$\Delta\psi_{QT,MAX} = k_c\left(\frac{D_{SAR}^2}{4r}\right) < \frac{\pi}{2}\ . \tag{3.10}$$

This limits the aperture size to

$$D_{SAR} < \sqrt{\frac{2\pi r}{k_c}} = \sqrt{r\lambda_c}\ . \tag{3.11}$$

When implementing the baseline version of DBS the above condition is assumed to be fulfilled, which gives the final expression for the phase difference,

$$\Delta\psi \approx -2k_c \left(\frac{x}{r}\right) \cdot u \ . \tag{3.12}$$

As seen in equation 3.12, the phase difference $\Delta\psi$ is linear proportional to the platform position u. Figure 3.5a shows the resulting linear functions for three different located scatterers: one at trailing edge (x<0), one at broadside ($x = 0$) and one at leading edge (x>0) assuming the platform is moving from $-D_{SAR}/2$ to $-D_{SAR}/2$.

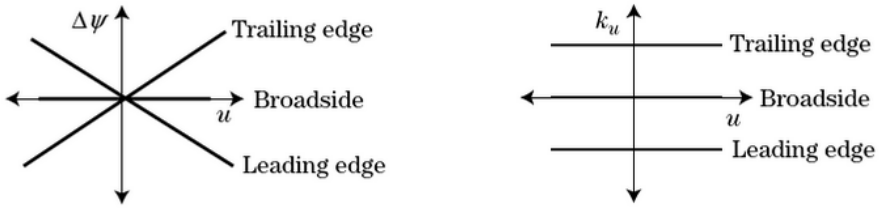

Figure 3.5: (a) shows how $\Delta\psi$ will change for a scatterer on the trailing edge, broadside and leading edge of the sensor respectively. The figure shows that the phase difference will be approximately linear. (b) shows the derivative of the phase for the three scatterers. This equals expressing the phase difference in the wavenumber domain.

The phase difference can also be examined by taking the derivative of $\Delta\psi$, which expresses the phase shift in the *spatial frequency* (or *wavenumber*) domain, meaning radians per unit distance. The derivative is given by

$$k_u \equiv \frac{\partial}{\partial u}\Delta\psi(u) \ . \tag{3.13}$$

The resulting function in wavenumber for the three scatterers can be seen in figure 3.5b. As seen in the figure the target at $x < 0$ will end up at $k_u > 0$, the target $x = 0$ ends up at $k_u = 0$ and the target at $x > 0$ ends up at $k_u < 0$. If the k_u-axis is flipped, the lines will correspond to the position of the scatterers, which is the purpose of DBS.

Summary

At the beginning of this section, DBS was simply explained as making a Fourier transform over each range bin. In the previous paragraph it was showed that the scatterer position could be related to the spatial frequency k_u. The spatial frequency can, in turn, be converted to frequency, which is the signals resulting domain after a Fourier transform,

$$f_d = -\frac{1}{2\pi}k_u v \tag{3.14}$$

where f_d is the resulting Doppler frequency and v is the platform velocity. The final step of the image formation after performing the Fourier transform is to map the resulting axes to distance.

However, the aperture limit presented in equation 3.11 implicitly restricts the image size, which is not always acceptable. To be able to collect data over a larger aperture, the quadratic phase error can be accounted for by applying a quadratic phase modulation to the data prior to DBS. This modulation is called an azimuth dechirp, and the process is referred to as *dechirping*. The aperture lengths in this thesis will often not fulfill the criteria in equation 3.11, and a dechirp will be applied to the data. Thus, when DBS is referenced throughout the thesis, it is implied that a dechirp has been applied prior to the Fourier transform, as long as nothing else is stated.

DBS is also possible to apply in the case of a 2-dimensional aperture. Instead of collecting samples along a linear track, samples can be collected in a plane consisting of several linear tracks parallel to each other. The only difference in implementing the algorithm is that a 2-dimensional FFT is used for the azimuth compression. However, this assumes that the samples are uniformly sampled in each aperture dimension.

There are certain limitations to consider when using DBS, some of which have been briefly mentioned in previous sections. First off, the track is assumed to be linear, and the samples are uniformly spaced. Secondly, the resulting image will be in slant range, and it is therefore assumed that the range to the target is much larger than the platform height above the ground plane so that cross-track approximately corresponds to down-range. Finally, DBS does not account for range migration. There are other algorithms that are commonly used to compensate for range migration but still operate in the frequency domain for effective computation. Two examples, which have been mentioned previously in section 2.3.5, are the *Range-Doppler Algorithm* [15], used in far-field scenarios, and the *Range Migration Algorithm* [16], often applied in near-field applications. Many variants of these algorithms have also been developed, e.g., [21], [22].

3.2 Image Evaluation

When evaluating images, the easiest method is to make a visual inspection. However, when comparing images, it is usually desired to have clearly defined metrics, such as numerical values. Two commonly used values are *contrast* and *entropy* [23],

$$I_{\text{Contrast}} = \sqrt{\frac{MN}{(\|\alpha\|_2)^2} \sum_{w=1}^{M} \sum_{q=1}^{N} |\alpha_{wq}|^4} \tag{3.15}$$

$$I_{\text{Entropy}} = -\sum_{w=1}^{M} \sum_{q=1}^{N} \frac{|\alpha_{wq}|^2}{(\|\alpha\|_2)^2} \ln\left(\frac{|\alpha_{wq}|^2}{(\|\alpha\|_2)^2}\right) \tag{3.16}$$

Here M and N correspond to the image rows and columns, respectively, and α represents the normalized pixel values. The contrast is the difference in image pixel values (color). The higher the contrast, the more distinguishable the image details become. An example

of a high contrast image is shown in Figure 3.6a. The image entropy is a measure of the system disorder and indicates the image's focus quality. The lower the entropy, the more focused the image is. Figure 3.6 illustrates the contrast and entropy for three different images. The corresponding values can be found in Table 3.1. The most desirable image is one with high contrast and low entropy, indicating visible and focused details.

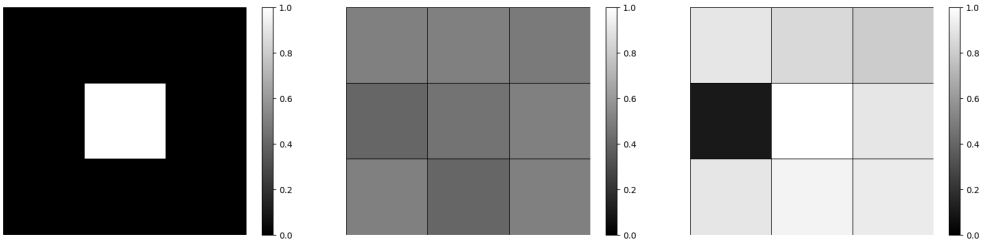

(a) High contrast, low entropy

(b) Low contrast, high entropy

(c) High contrast, high entropy

Figure 3.6: Shows three 3×3 images illustrating the concepts of contrast and entropy where a white pixel is 1 and a black pixel is 0.

Table 3.1: Shows the corresponding values for contrast and entropy for the figures in figure 3.6.

	I_{Contrast}	I_{Entropy}
(a)	3.00	0.00
(b)	1.44	2.19
(c)	2.82	2.15

Chapter 4

Simulations

The following chapter will present images of a simulated point scatterer generated using both Doppler Beam Sharpening and Global Backprojection. The aim of the chapter is to demonstrate the differences between the two methods and illustrate the effects of both dechirping and range migration for DBS.

The second part of the chapter consists of simulations with added errors and noise to exemplify how these affect the final image. The purpose is to give the reader an intuitive understanding of how different noise-induced effects manifest in the images.

The simulation consists of a point scatterer placed in the near-field at broadside and at a range of 0.25 m. The aperture is one-dimensional and placed at the same height as the scatterer, ensuring that the slant-range and down-range are equal to each other. The half-power beam width is set to 29.2 degrees to simulate the beamwidth of the A121 sensor. The beam is simplified to have the shape of a rectangular window, meaning all data inside the beam is equally attenuated, and the data outside the beam is set to 0. The aperture is sampled every $\lambda/4$, and the aperture length is calculated using Equation 2.10 with r equal to 0.25 m. The wavelet used as the received signal is a Gaussian function with a FWHM of 0.03 m and a carrier frequency of 60.5 GHz (see Figure 4.1). The wavelet is sampled at discrete distance intervals of 2.5 mm to simulate the data points in a sweep of the A121 sensor.

Figure 4.2 shows the energy and phase of the raw data for the scatterer, along with the resulting images using backprojection and DBS. The energy plot displays the normalized squared amplitude of of each sweep in dB-scale. The yellow color (0 dB) indicates at which range, in that sweep, most energy is registered. This range corresponds to the distance between the scatterer and the sensor at that position index along the collection path. The sweeps at position index 0 and position index 110 will indicate a slightly longer range to the scatterer compared to position index 55 since these positions are further from the point scatterer. The phase plot in Figure 4.2 below have the same axes but instead of displaying the energy, the phase for each sweep in degrees is depicted.

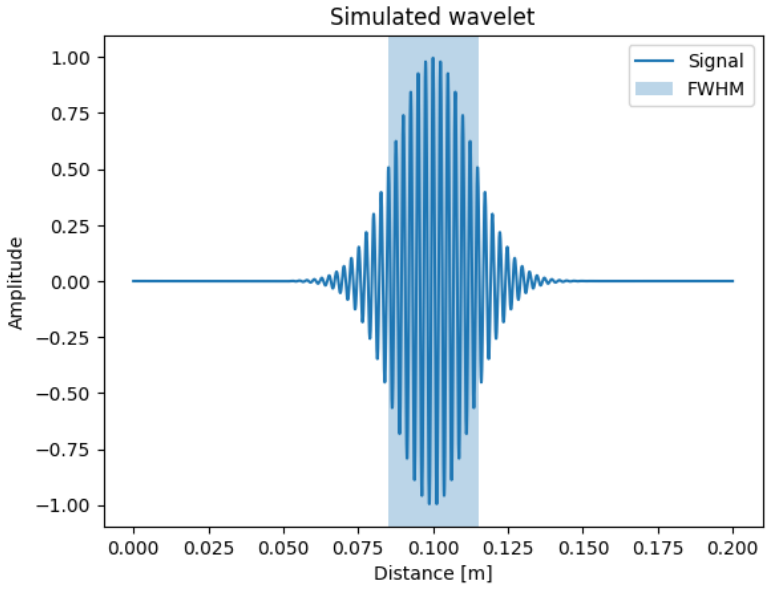

Figure 4.1: Shows the wavelet used as the received signal in the simulations. It has a carrier frequency of 60.5 GHz and a FWHM of 0.03 m to simulate the signal created by the A121 sensor.

Bear in mind that all points have some phase and some energy despite the energy plot showing only energies down to -20 dB.

In the energy plot of Figure 4.2, a slight curvature can be seen, indicating range migration, which is expected for a scatterer located in the near-field. However, an even clearer indicator of the scatterer's near-field location is the phase. For a scatterer located in the far-field, the received signal can be approximated as a plane wave, implying that the phase would be 0 for the entire range bin in which the scatterer is located, presumed that the scatterer were at broadside. However, in this figure, as seen in the phase plot, the phase has a parabolic shape instead, which indicates that the plane wave approximation is not viable and that the position index along the aperture affects the phase in the received signal.

Furthermore, both backprojection and DBS successfully depict the scatterer at the correct location. The azimuth resolution of the scatterer is better than the range resolution, since the main lobe is more narrow in azimuth than in range, which aligns with the theory presented in Section 2.3.3. Both images exhibit sidelobes as a result of azimuth compression, but the sidelobes are small compared to the main lobe. The contrast and entropy of the images can be viewed in Table 4.1. The contrast is slightly higher and the entropy is slightly lower for the backprojected image, indicating that the image is marginally more focused.

Table 4.1: Contrast and entropy for the images shown in Figure 4.2

	Contrast	**Entropy**
Backprojection	163.3	5.9
DBS	162.6	6.0

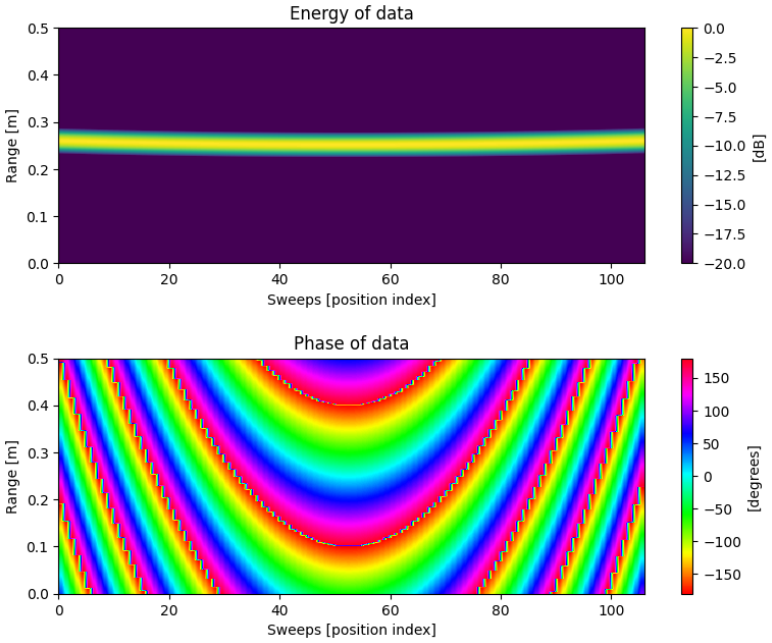

(a) Energy and phase of raw data

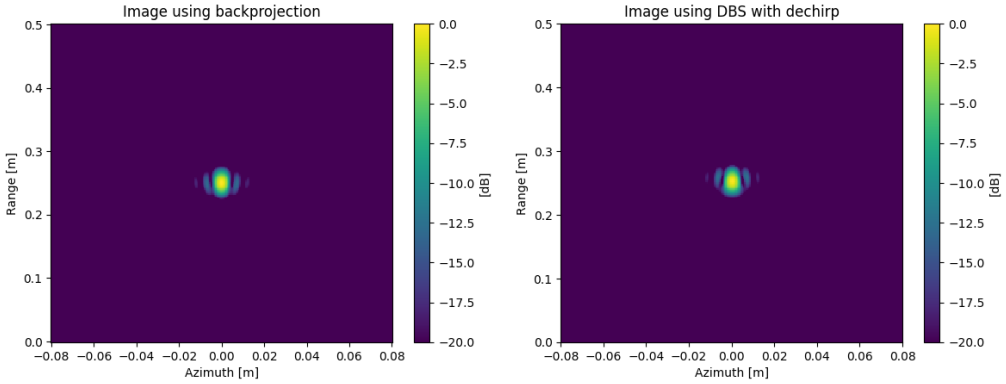

(b) Image using backprojection

(c) Image using DBS

Figure 4.2: (a) Simulated raw data from collection of a one-dimensional aperture where the target is a point scatterer located at 0.25 m in range; (b) and (c) shows the resulting images using backprojection and DBS, respectively.

4.1 Doppler Beam Sharpening

This section will illustrate the impact of dechirping the signal before applying DBS and the effects of range migration.

4.1.1 Effect of Dechirping

Dechirping was previously described in Section 3.1.2, where it was defined as the process of applying a quadratic phase modulation to the data prior to DBS. The purpose of dechirping is to compensate for the phase change caused by the change in distance to the scatterer when the sensor is moved along a long aperture. Figure 4.3 shows the difference between not dechirping and dechirping the data. Figure 4.3a shows the same energy and phase plot as in Figure 4.2a. However, Figure 4.3b shows the DBS image generated directly from this data without first applying the dechirp factor as previously. Figure 4.3c shows the raw data after dechirping and Figure 4.3d shows the resulting DBS image on this data. Note that Figure 4.2c and Figure 4.3d shows the same image but with different length on the x-axis. The axis is changed in Figure 4.3d to highlight the difference between dechirping and not dechirping.

In the phase plot shown in Figure 4.3a, the quadratic phase change is clearly visible as the parabolic shape of the phase lines. Applying DBS directly to this data results in the point scatterer being imaged as very wide (see Figure 4.3d). This is because the derivative of the phase change within the range bin includes both positive and negative values, which results in a wide spectrum of included spatial frequencies, which in turn results in a wide depiction of the point scatterer. After applying the dechirp, the phase is flattened within the range bin where the scatterer is located since the dechirp factor compensates for the quadratic phase change caused by a long aperture (see Figure 4.3c). This results in a much better azimuth resolution of the scatterer, as shown by the more narrow depiction in Figure 4.3d. Since the dechirp factor only compensates for the phase change in the signal, the energy of the signal will remain unaltered.

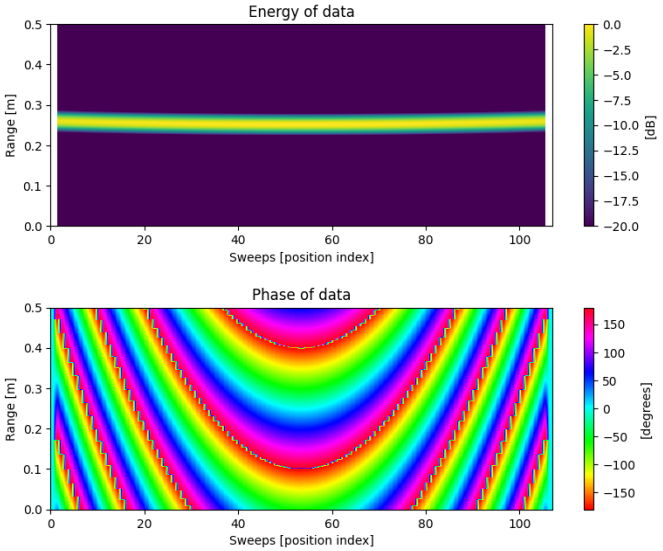

(a) Energy and phase of raw data

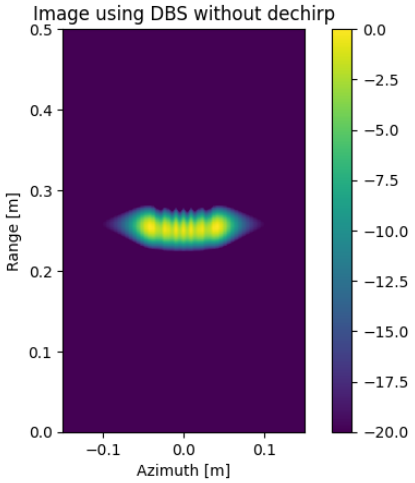

(b) Image using DBS without dechirp

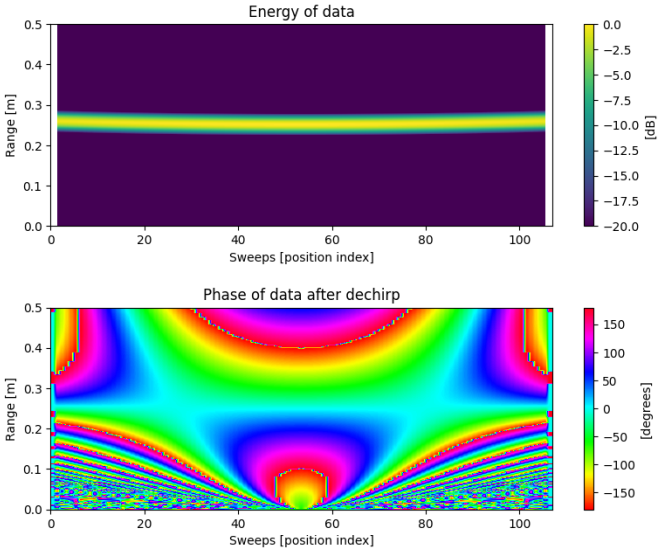

(c) Energy and phase of raw data after dechirping

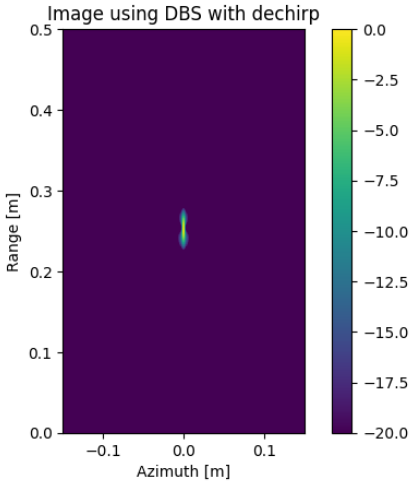

(d) Image using DBS with dechirp

Figure 4.3: (a) Simulated raw data from collection of a one-dimensional aperture where the target is a point scatterer located at 0.25 m in range; (b) shows the resulting image of applying DBS on the raw data; (c) shows how the phase changes after applying the dechirp; (d) shows the resulting image using DBS on this data.

4.1.2 Effect of Range Migration

In the previous images, there was only a slight curvature in the energy plot as the position index changed. Consequently, it has been challenging to notice the range migration in

the resulting images. Since the simulated half-power beam width is only 29.2 degrees, the resulting aperture length is short (seen from a range migration perspective). This leads to a minimal difference in distance to the scatterer between the position at $u = 0$ (the position closest to the scatterer) and $u = D_{SAR}/2$ (the position at the end of the aperture). Figure 4.4 depicts the same scatterer as before, but with an increased half-power beam width of 70 degrees. This results in a larger aperture and a more pronounced range migration, as the energy is distributed across more range bins (see Figure 4.4a). In the resulting DBS image (see Figure 4.4c), the effect of range migration becomes clearly observable, with energy spread across multiple range bins and prominent sidelobes.

When examining the image generated with backprojection in Figure 4.4b, it remains unaffected by range migration. Instead, the image appears more focused, which is a result of the longer aperture.

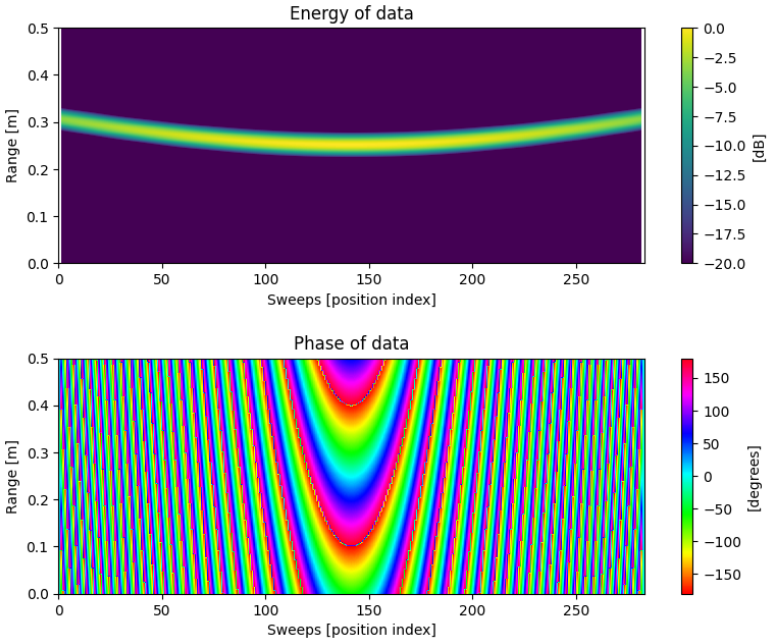

(a) Energy and phase of raw data

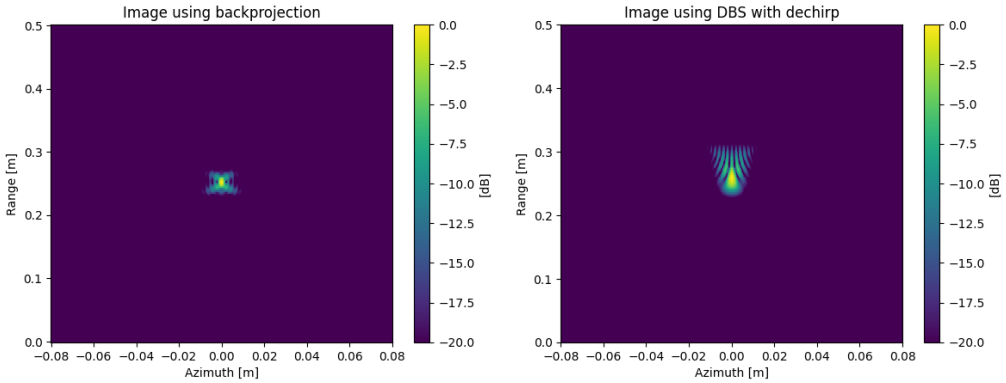

(b) Image using backprojection

(c) Image using DBS

Figure 4.4: (a) Simulated raw data from collection of a one-dimensional aperture where the target is a point scatterer located at 0.25 m in range with a half-power beam width of 70 degrees; (b) and (c) shows the resulting images using backprojection and DBS, respectively.

4.2 Effects of Noise and Errors on Imaging

The following section illustrates how white noise, range error and azimuth error affects the images.

4.2.1 White Noise

The purpose of adding white noise to a signal is to see how the image is affected by a low *signal-to-noise ratio* (SNR). SNR in decibel is defined as

$$\mathrm{SNR}_{\mathrm{dB}} = 10 \cdot \log\left(\frac{\text{signal power}}{\text{noise power}}\right) \tag{4.1}$$

For a white noise process, the SNR is given by $\frac{1}{V[\text{noise}]}$, where $V[\text{noise}]$ represents the variance of the noise process, assuming that the maximum signal power is 1. In the simulations the noise is added onto the normalized raw data, which in normalized by the maximum of the entire raw data matrix.

Figure 4.5 displays raw data with an SNR of 0.1. The energy plot exhibits high noise levels, making it challenging to visually distinguish the signal. However, when examining the resulting images, the scatterer can still be perceived using both algorithms, albeit with noticeable noise. The reason behind the scatterer's visibility in the images, is the correlation utilized by both algorithms in the azimuth compression. Since white noise is uncorrelated, the correlated data corresponds to the scatterer.

Figure 4.6 illustrates the dependence of image entropy and contrast on SNR. As expected, entropy decreases as SNR increases. At very low SNRs, the contrast is high, decreasing rapidly and then gradually increasing for both algorithms. The high contrast at low SNRs is caused by the elevated energy in the noise speckles. As SNR increases, the noise power decreases, resulting in a decrease in image contrast. With further increases in SNR, more power concentrates at the location of the point scatterer, causing the contrast to slowly increase again.

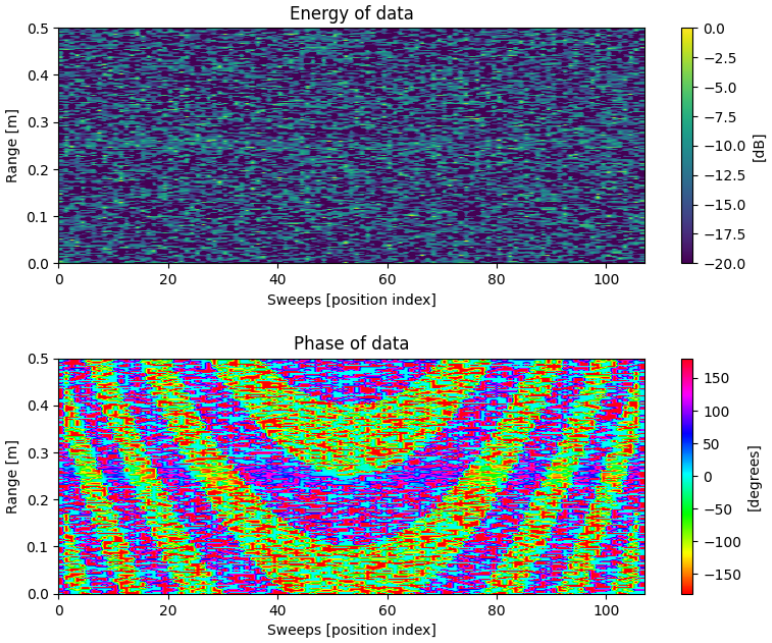

(a) Energy and phase of raw data

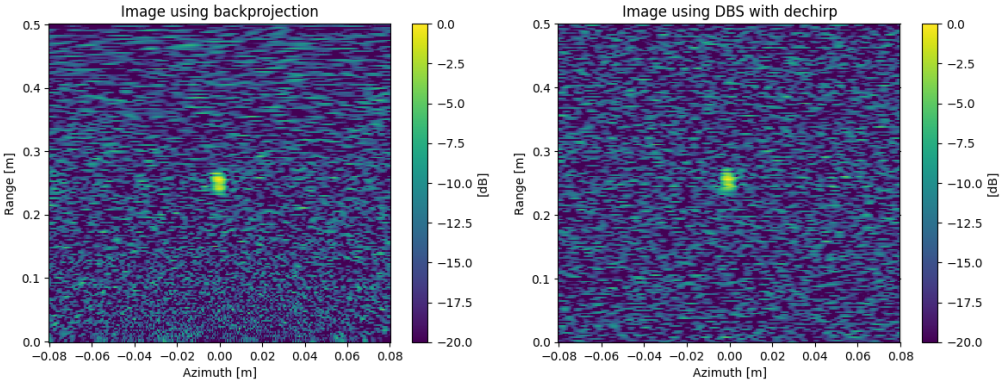

(b) Image using backprojection

(c) Image using DBS

Figure 4.5: (a) Simulated raw data from collection of a one-dimensional aperture where the target is a point scatterer located at 0.25 m in range with a SNR of 0.1. (b) and (c) shows the resulting images using backprojection and DBS, respectively.

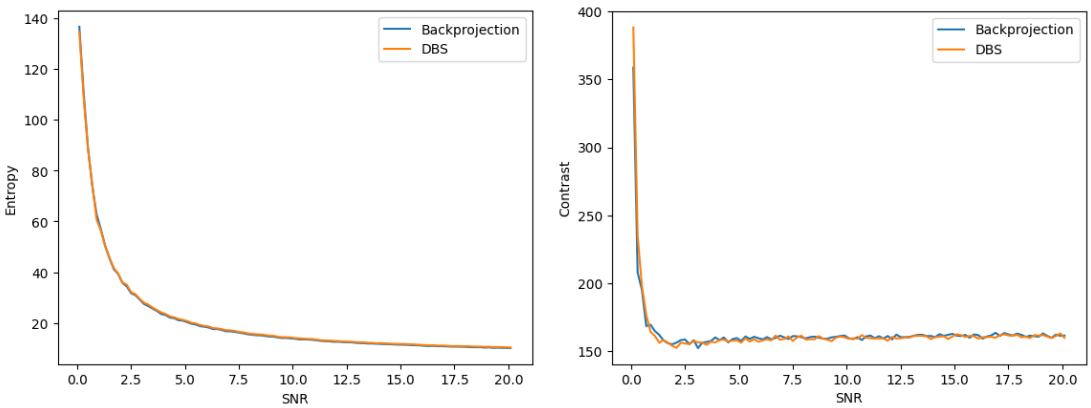

(a) Entropy

(b) Contrast

Figure 4.6: Image entropy and contrast as a function of SNR. The graphs are a mean over 5 runs.

4.2.2 Range Error

This section introduces a range error into the data. The range error can be seen as a wiggle perpendicular to the aperture. When applying the algorithms, the aperture is assumed to be straight, but in reality, the data points are collected slightly off the aperture. As a result, the perceived distance to the scatterer differs from the actual distance. The range error for each position index follows a normal distribution with an expected value of 0 and a standard deviation expressed in terms of the number of wavelengths. The effect of a noticeable range error can be seen in the raw data in Figure 4.7a where the energy plot exhibits slight fluctuations, however, the effect can most clearly be discerned in the phase plot where the previous parabolic pattern is now indistinguishable.

Figure 4.7 illustrates the data and final images with a range error of 0.12 λ. The point scatterer is just barely distinguishable from the error artifacts in the resulting images. In the backprojection image, the artifacts are spread across more range bins compared to the DBS image. However, the energy of the artifacts in the backprojected image is lower compared to the main peak when compared to the DBS image. Since the energy in the artifacts in the backprojected image is lower they would be easier to filter out by, for example, applying an energy threshold to the images. This observation is also reflected in Figure 4.8, which depicts the relationship between entropy, contrast, and range error for the two methods. The figure shows a higher entropy and contrast in the backprojected as the error increases, compared to the DBS image. This outcome is expected due to the nature of the algorithms: backprojection can project energy to all pixels in the image, whereas DBS only performs an FFT along the range bins, restricting the energy to the range bins where it is present in the raw data. The artifacts will therefore be spread over more pixels for the backprojected image but contain less energy.

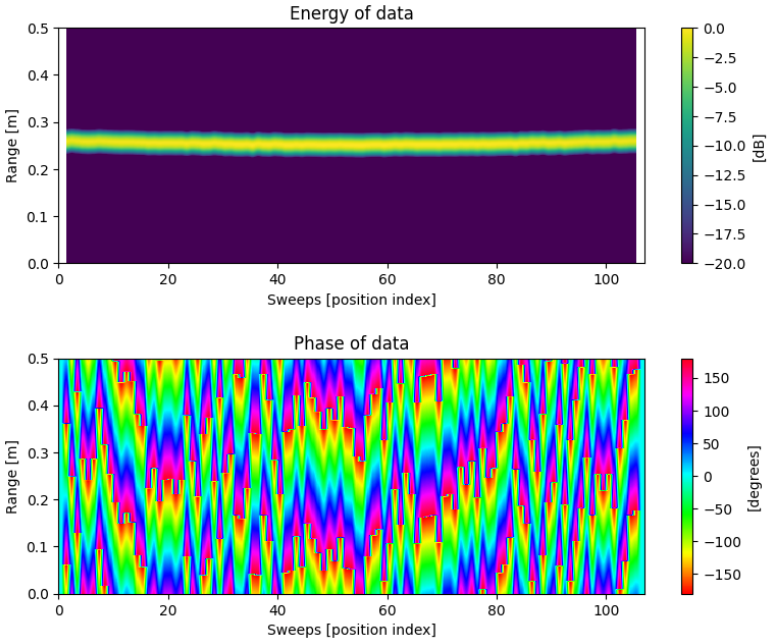

(a) Energy and phase of raw data

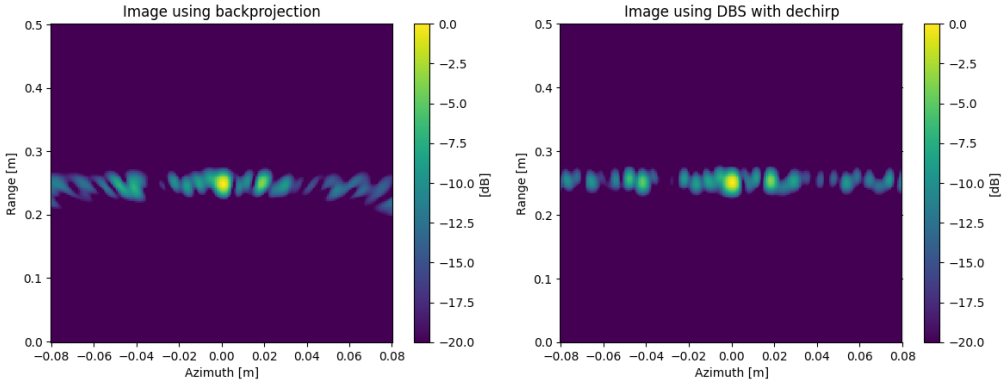

(b) Image using backprojection

(c) Image using DBS

Figure 4.7: (a) Simulated raw data from collection of a one-dimensional aperture where the target is a point scatterer located at 0.25 m in range with a range error with standard deviation of 0.12 λ (b) and (c) shows the resulting images using backprojection and DBS, respectively.

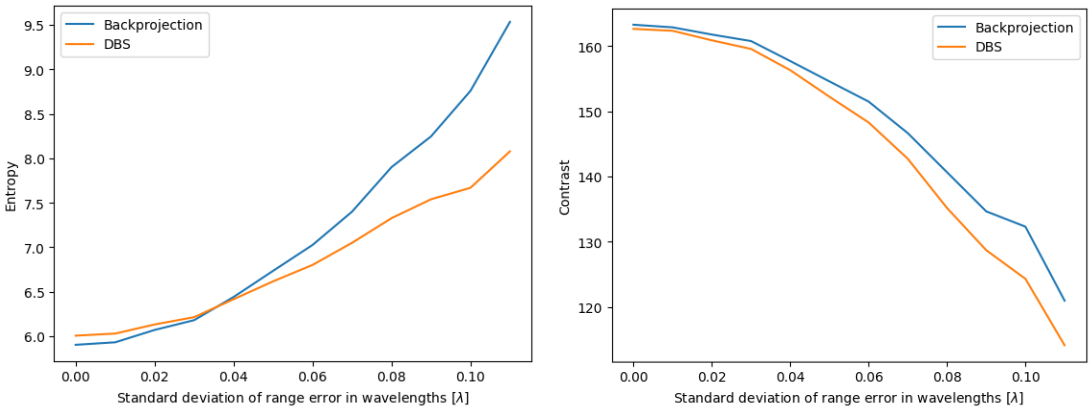

(a) Entropy

(b) Contrast

Figure 4.8: Image entropy and contrast as a function of range error. The range error is defined by the standard deviation given in wavelengths. The graphs are a mean over 10 runs.

4.2.3 Azimuth Error

The azimuth error is simulated in the same way as the range error, but instead of introducing a wiggle perpendicular to the aperture, the wiggle is now along the aperture.

The raw data and final images can be viewed in Figure 4.9. Figure 4.9a shows the energy and phase of the raw data with an azimuth error of 1λ. The energy plot exhibits small fluctuations, just as for the range error. However, the phase plot displays more disruptions to the parabolic pattern at the edges of the aperture than in the middle. The reason that the pattern is still noticeable in the middle of the aperture is that, for a scatterer located at broadside, the phase is approximately the same for all positions around $u = 0$ (the aperture position closest to the scatterer). Introducing an error in azimuth around this point will have less effect on the phase than a range error introduced around the same position. The error will, however, still manifest itself in the images by both displaying artifacts and widening the main lobe in azimuth direction.

The error artifacts in Figures 4.9b and 4.9c are located in the same manner as for the images with the range error (see Figures 4.7b and 4.7c), where the artifacts are spread over several range bins for the backprojected image while the DBS artifacts are located in fewer range bins but the artifacts contain more energy. This is also shown in the behaviour of the entropy and contrast plots in Figure 4.10 as azimuth error increases. Where the entropy and contrast for the backprojected image is greater than for the DBS image implying that the backprojected image has a more distinguishable main lobe but with less focus.

Comparing the resulting images in Figures 4.7 and 4.9, one can notice that the point scatterer is much more distinguishable in the images containing the azimuth error, even though the error is much larger (1λ for the azimuth error compared to 0.12λ for the range error). This is most likely due to a combination of a higher sampling rate in the azimuth direction ($\lambda/4$) compared to the sampling rate in range ($\lambda/2$), and the phase difference caused by the error. As seen in Figure 4.9a the phase pattern is still discernible in the middle of the aperture at an error of 1λ compared to Figure 4.7a with an error of only 0.12λ. In conclusion, the tolerance for errors is higher in the azimuth direction compared to the range direction.

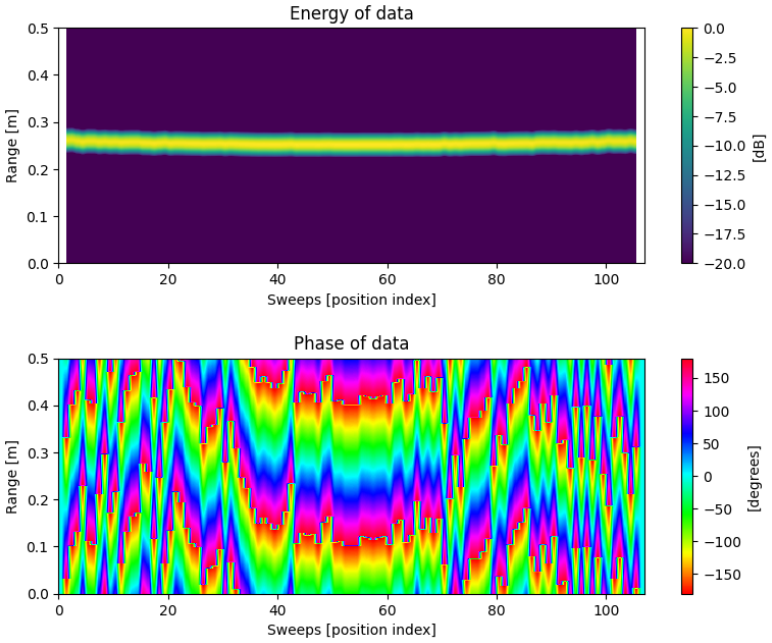

(a) Energy and phase of raw data

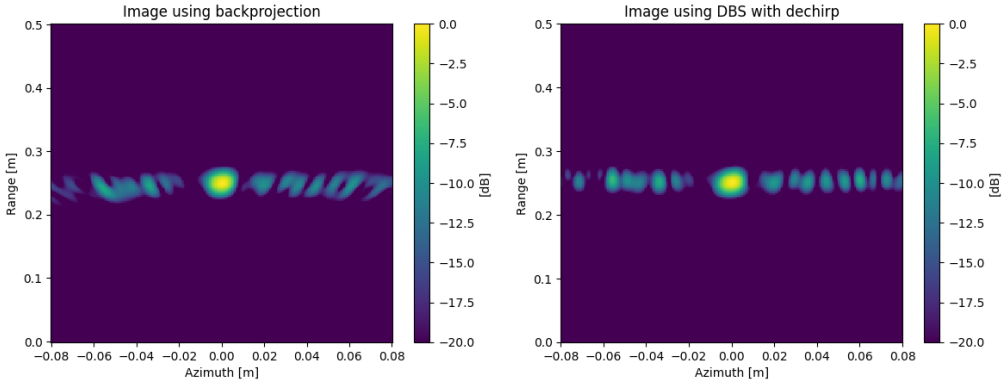

(b) Image using backprojection

(c) Image using DBS

Figure 4.9: (a) Simulated raw data from collection of a one-dimensional aperture where the target is a point scatterer located at 0.25 m in range with a azimuth error with standard deviation of 1 λ (b) and (c) shows the resulting images using backprojection and DBS, respectively.

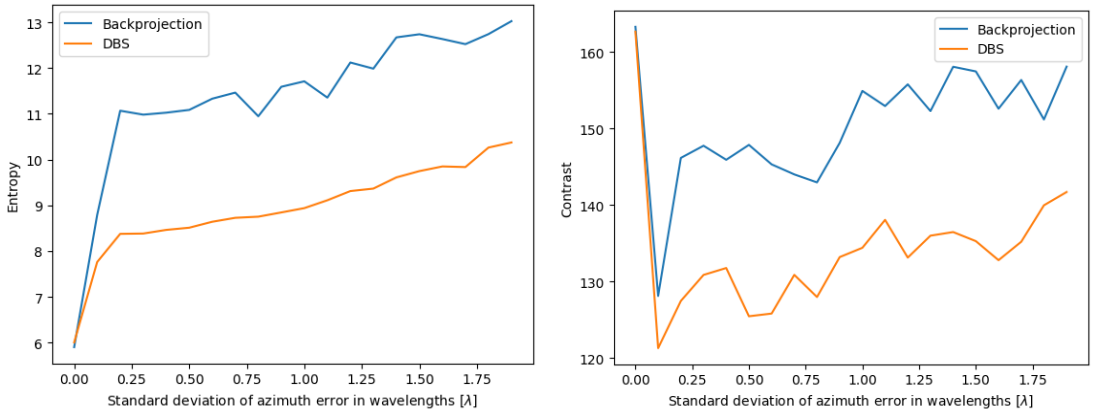

(a) Entropy

(b) Contrast

Figure 4.10: Image entropy and contrast as a function of azimuth error. The azimuth error is defined by the standard deviation given in wavelengths. The graphs are a mean over 10 runs.

Chapter 5

Measurements

This chapter will showcase SAR images generated by data collected with the A121 sensor. The first section will provide a more detailed description of the sensor, while the subsequent sections will present the resulting images using both Global Backprojection and Doppler Beam Sharpening. Both one- and two-dimensional apertures will be utilized to demonstrate the effect of adding an additional dimension to the data.

The aim of this chapter is to connect the theory to real measurements and exemplify the possibilities of near-field SAR imaging using relatively simple algorithms.

5.1 Acconeer's A121 sensor

The A121 sensor, which was breifly introduced in Section 2.2, is a single channeled (one Tx-antenna and one Rx-antenna) PCR system with a center frequency of 60.5 GHz. The antennas are included in the package and the package size is 5.5×5.2 mm. Figure 5.1a shows the sensor and Figure 5.1b shows the corresponding antenna planes. The aim of the PCR technology is to attain high precision readings with low power consumption.

In Section 3.1, the SAR image formation algorithms were assumed to be divided into two steps: range compression and azimuth compression. While the azimuth compression is often considered algorithm-specific, the range compression is system-specific. In the case of this radar system, the range compression is performed directly in the hardware, resulting in the output data already being range compressed. When the received pulse is sampled, it is convolved with an identical pulse to the transmitted one, effectively creating a matched filter for the received signal ensuring range compression. For the pulse length used in the following measurements, the FWHM of the range-compressed signal is approximately 0.03 m.

The A121 sensor has various integrations. For the measurements conducted in this thesis, a satellite card with the A121 sensor (XS121) was used in conjunction with the XE121 evaluation kit. The beam widths for the sensor differ slightly between different

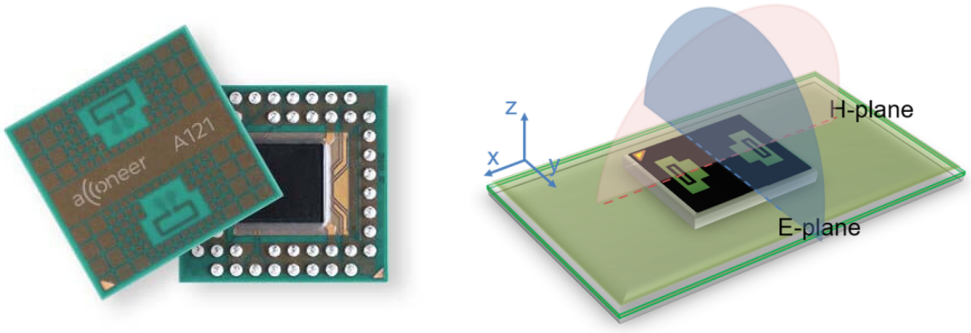

(a) **(b)**

Figure 5.1: (a) Shows the front and backside of Acconeer's A121 sensor which is used in the thesis (Image source: [24]). (b) shows the antenna planes in relation to the sensor (Image source: [6])

integrations. For the XS121, the beam width for the two antenna planes can be observed in Figure 5.2. The half-power beam width for the E-plane is 29.2 ± 2.33 degrees, and for the H-plane, it is 41.2 ± 9.33 degrees.

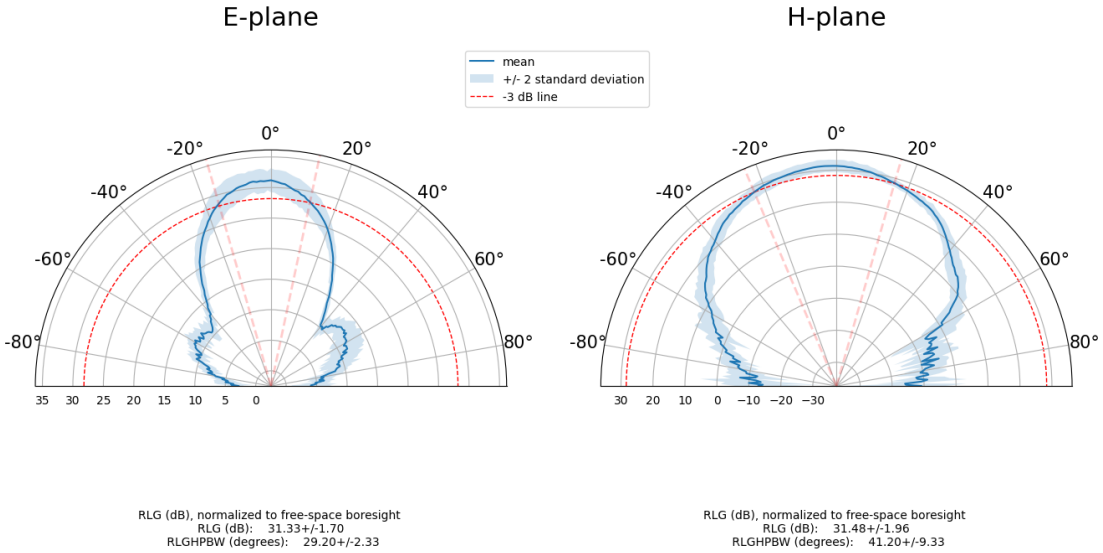

Figure 5.2: Shows the half-power beam width for the XS121 (The satelite-card using the A121 sensor).

5.2 2D SAR images

In the following section, two-dimensional SAR images are generated using data collected along a one-dimensional collection path. The objective is to create an image of batteries arranged in a pattern forming the letters "EY" (see Figure 5.3b). The experimental

setup can be seen in Figure 5.3a, where the sensor is positioned beneath the black block with a look angle of 30.3 degrees towards the floor. The sensor is placed on a height of 1.2 m, with an approximate distance to the scene of 1.4 m. The collection path has a length of 0.4 m and is sampled at intervals of 1.25 mm. The sensor remains stationary during both transmission and reception at each measurement point along the aperture. This methodology ensures that the stop-and-hop approximation is no longer an approximation but rather an accurate representation of the data acquisition process. The sensor settings used for the data collection can be found in Table 5.1, which lists the configurable parameters for the A121 sensor. The start point and number of points were chosen to fit the entirety of the scene.

Table 5.1: A121 sensor settings used during data collection

Profile	1
HWAAS	20
Receiver gain	16
Phase enhancement	True
Step length	1
Start point	496
Number of points	127

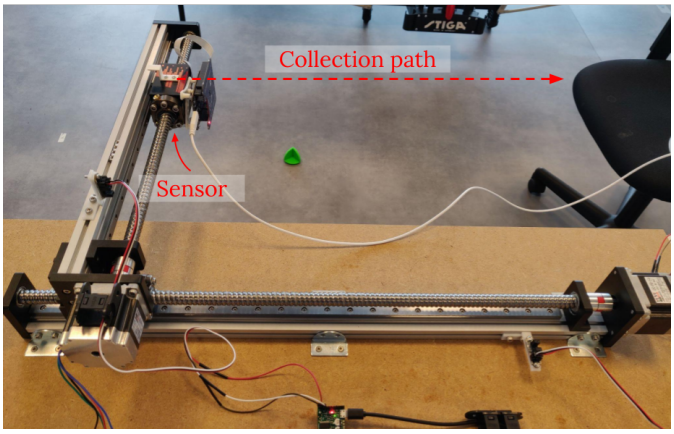

(a)

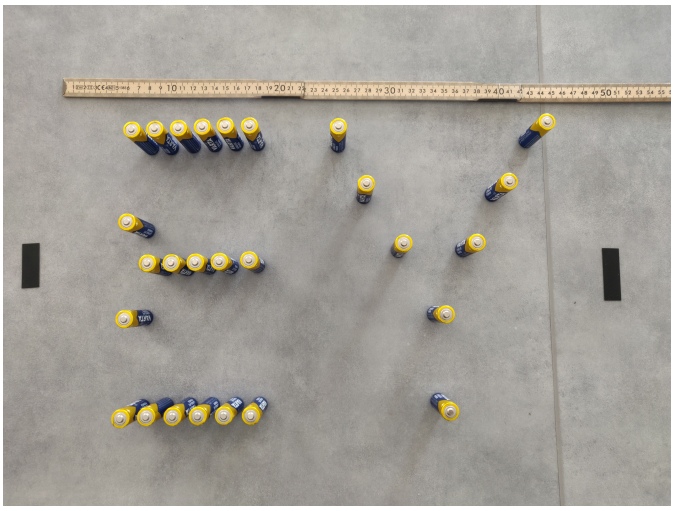

(b)

Figure 5.3: (a) Shows the collection path for the system. The sensor is located underneath the black block with a look angle of 30.3 degrees. The corner reflector shows where the scene is located; (b) shows a close up of the scene that should be imaged. The target are batteries placed in the shape of the letters "EY".

The batteries forming the "E" are positioned at the theoretical resolution limit for the image. The azimuth resolution is determined by Equation 2.15, taking into account the half-power beam width of 29.2 degrees, resulting in a resolution of 4.9 mm. The horizontal distance between the batteries is set to this distance, measured between the edges of the batteries. The down-range resolution is calculated using Equation 2.8, where the range resolution for the system corresponds to the FWHM of the signal (0.03 m). In this setup, the theoretical down-range resolution is 0.062 m, representing the vertical distance between the batteries in the leftmost column (see to Figure 5.3b).

The raw data obtained from the measurements is displayed in Figure 5.4. It is evident

that the data contains more noise and scatterers compared to the simulated images presented in the previous chapter, as is expected in measured data.

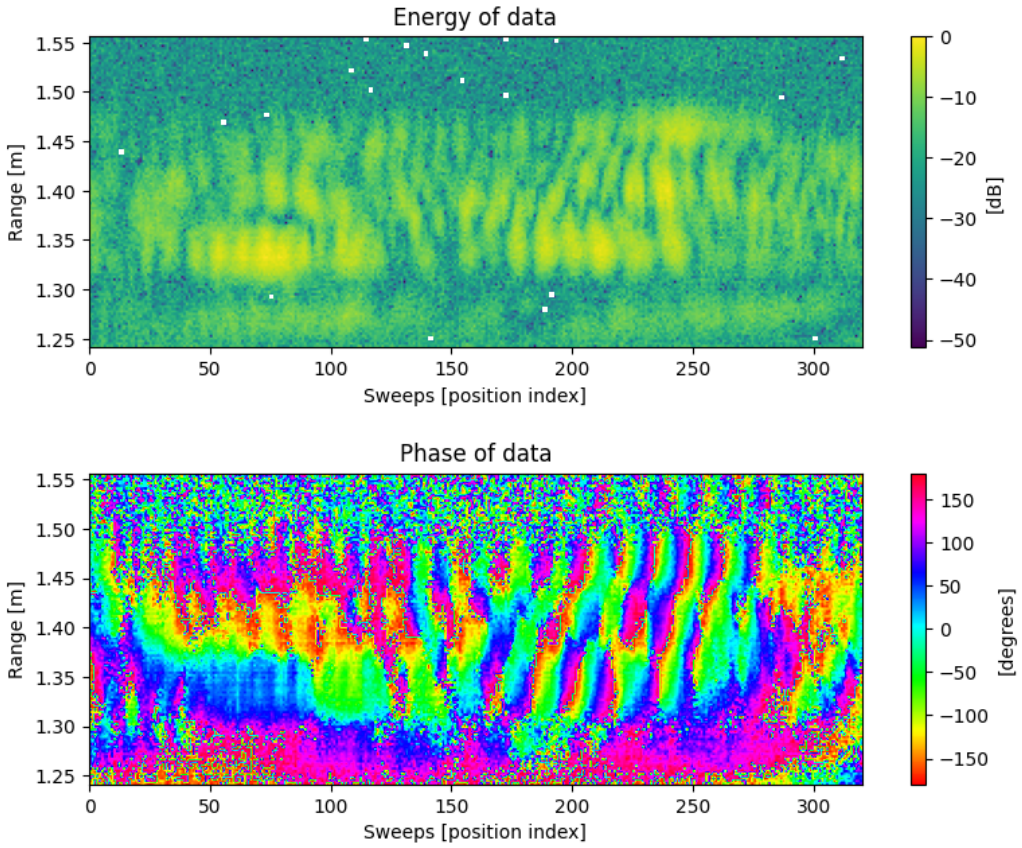

Figure 5.4: Raw data from collection of a one-dimensional aperture. Energy of the data is in the top plot and the phase of the data in degrees are in the second plot. The image can be seen as the sensor being moved from left to right, where each column is the data for a sweep.

The resulting images using DBS can be seen in Figure 5.5. The figure includes four variations of the DBS image. The top left plot displays the image without dechirping, and the "EY" pattern is indistinguishable. In the bottom left plot, the data was dechirped before applying DBS, and now the pattern becomes observable. In the plots on the right, a Hanning window with a width of 0.1 m was applied to the data, effectively reducing the aperture length to 0.1 m. As expected according to theory, the azimuth resolution becomes coarser. However, the rough shape of the pattern can still be slightly perceived. It is also worth noting that the effect of dechirping the windowed data is minimal. This phenomenon arises because the phase is largely unaffected by the distance change to the targets when the sensor is moved between positions at the center of the aperture, rendering the dechirping process redundant. This observation aligns with the theory presented in Section 3.1.2, which states that for short apertures, the impact of

the quadratic phase function is negligible.

One should also note that in these images, the dechirp is applied separately for each range bin. The reason is that the range interval of the images is comparable to the distance to the scene. The dechirp applied to the range bins closest to the aperture differs significantly from the dechirp applied to the bins furthest away in the image. However, if the range interval of the image were much smaller than the distance to the scene, it could be acceptable to apply the same dechirp to all range bins. This approach would save computational resources, so it is worth considering if one wants to reduce the computational complexity of the method.

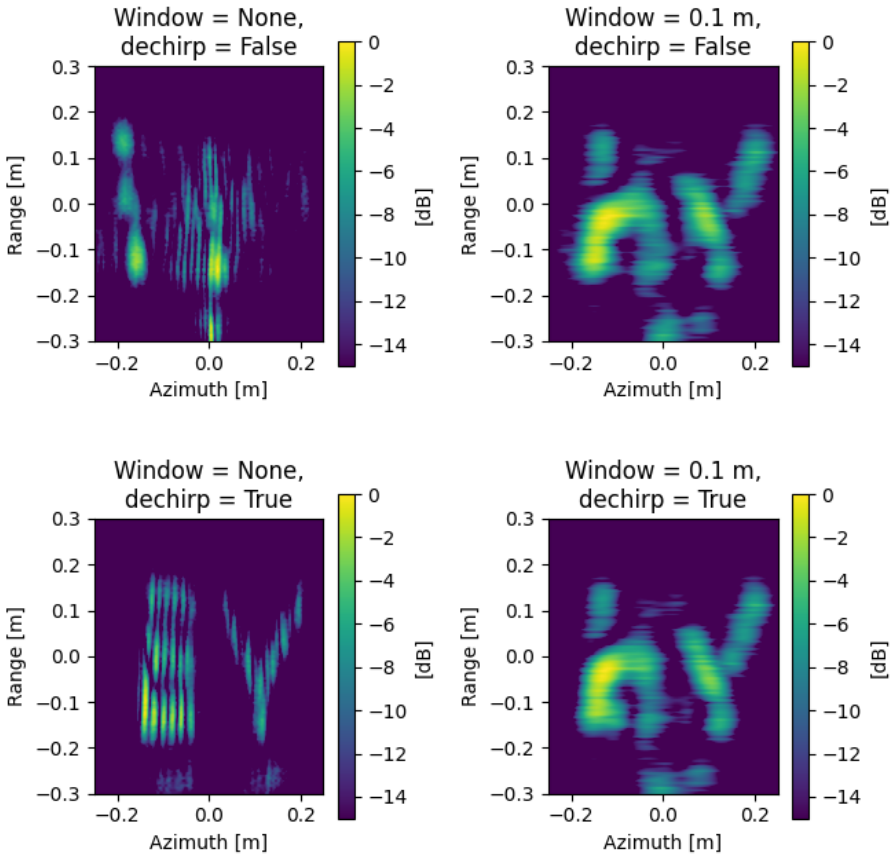

Figure 5.5: The resulting SAR-image using DBS on data collected on a 0.4 m aperture with a step length of 1.25 mm, a height above ground of 1.2 m and a slant range to the scen centre of approx. 1.4 m. The look-angle was 30.3 degrees. The four images illustrates the impact of a shorter aperture (applied window to data) and the effect of the dechirp factor. The applied window is a Hanning window of width 0.1 m. The image is depiced in slant-range.

In Figure 5.6, the image obtained using backprojection can be viewed. There is no noticeable difference between the backprojected image and the dechirped non-windowed

version of the DBS image. In both the backprojection and DBS images, almost every individual battery can be distinguished, except for the two batteries on the bottom left of the "E" and the two at the bottom of the "Y". This is most likely due to the fact that the down-range resolution was calculated for the center of the scene. The look-angle for the closest part of the scene is smaller than 30.3 degrees, resulting in a coarser resolution limit. It is important to remember that the resolution limits are based on several approximations, making it challenging to achieve the exact theoretical resolution in a real scenario.

Another observation that can be made from the images is the presence of artifacts near the bottom edge of the picture. These artifacts are likely caused by reflections from the batteries onto the floor.

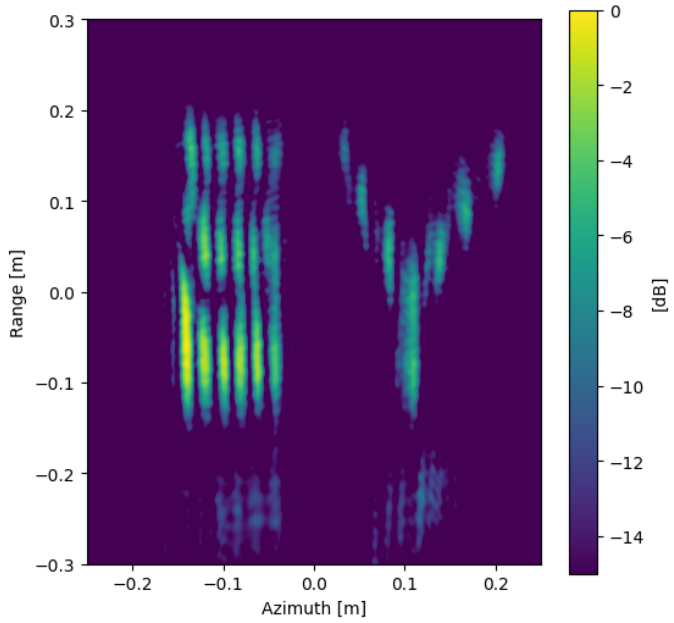

Figure 5.6: The resulting SAR-image using global backprojection on data collected on a 0.4 m aperture with a step length of 1.25 mm, a height above ground of 1.2 m and a slant range to the scen centre of approx. 1.4 m. The look-angle was 30.3 degrees. The image is depicted on the ground plane.

5.3 3D SAR images

In this section, a two-dimensional aperture is employed to generate a 3D SAR image. The setup can be observed in Figure 5.7, where scissors was utilized as the target object. The sensor was moved in a Z-pattern, as depicted in Figure 5.8, creating an aperture matrix. The step length in both elevation and azimuth was set to 1.25 mm ($\sim \lambda/4$). The pattern covers an area of 0.15×0.20 m, resulting in 120×160 sampling positions along the collection path. The sensor was positioned with the E-plane parallel to the azimuth

direction and the H-plane parallel to the elevation direction.

Table 5.2: A121 sensor settings used during data collection

Profile	1
HWAAS	16
Receiver gain	16
Phase enhancement	True
Step length	1
Number of points	33

As depicted in the figures, the scissors were positioned on a styrofoam-like block. This setup aims to simulate a pair free-floating scissors, as the white block reflects minimal to no 60 GHz EM waves, rendering it nearly invisible to the current radar system. The measurements were conducted at two different distances to the scissors: approximately 0.25 m and approximately 0.12 m. However, both positions fall within the near-field region. The purpose of this is to examine how the target distance impacts the output of the two algorithms. According to theory, the DBS algorithm should exhibit artifacts in the image due to range migration at sufficiently close distances, whereas the backprojected images should remain unaffected. The A121 sensor settings employed during data collection can be found in Table 5.2. The start point parameter is intentionally omitted from the table, as it depends on the distance to the desired target.

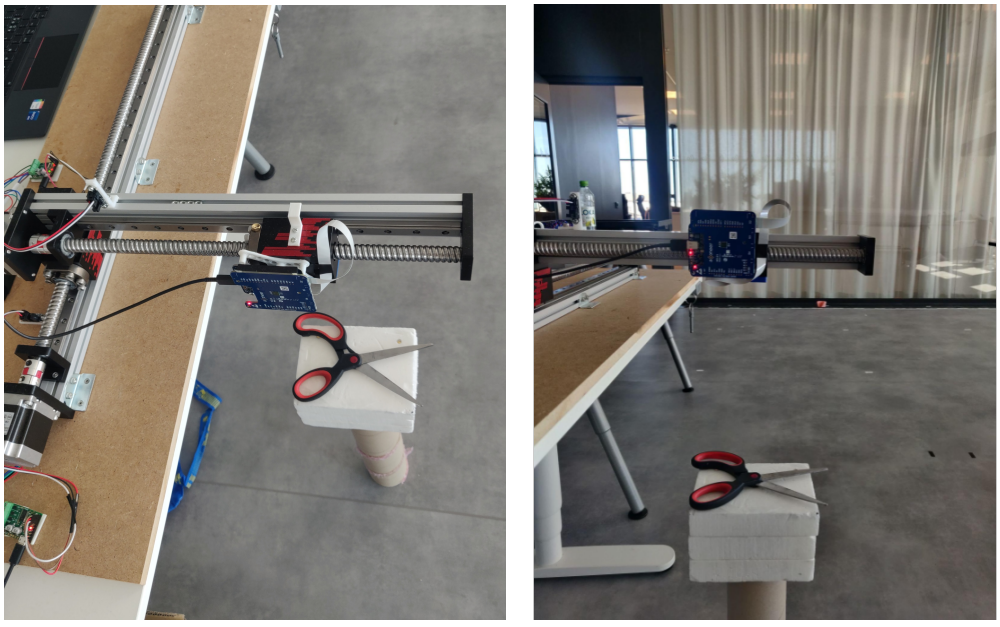

(a) **(b)**

Figure 5.7: The 3D SAR setup. The sensor can be moved in two direction using two linear stages. The sensor is located underneath the black block looking straight down on the scissors.

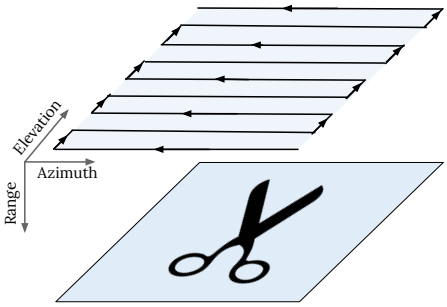

Figure 5.8: Illustrates the collection path used during the measurement of the scissors.

The 2D and 3D representations of the results obtained with the scissors positioned at a distance of 0.25 m from the sensor are presented in Figure 5.9. The 2D images correspond to the slices of the 3D images exhibiting the highest pixel variance, indicating the slices with the highest energy. Due to the distinct operating mechanisms of the two algorithms, the slice with the highest energy will be located at different ranges. The backprojection 2D image is the slice at 0.2575 m and the DBS 2D image is the slice at 0.2627 m, which would be a contributing factor as to why the prominent details differ between the images, such as the screw connecting both blades.

Both images clearly depict the blades of the scissors, which are easily discernible. Since they are metallic objects positioned perpendicular to the radar pulses, they act as effective scatterers, making them favorable targets for SAR imaging. Conversely, the handles of the scissors, composed of plastic material, do not exhibit the same scattering characteristics. Due to the dispersion of the pulses within the plastic material, less energy is reflected back to the sensor. This disparity is evident in both images, as the handles appear fainter and gaps in the structure are noticeable.

Since the aperture is sampled in both azimuth and elevation, it is assumed that the resolution is high in both dimensions. According to Equation 2.15, the elevation resolution can be as good as 3.4 mm, while the azimuth resolution can reach 4.9 mm. The difference in resolution between the dimensions arises from the difference in half-power beam width between the E-plane and H-plane. However, the range resolution is determined by the FWHM of the range-compressed pulse, which measures 0.03 m. This discrepancy is noticeable in the 3D image, where the scissor appears elongated in the range dimension. Therefore, the orientation of the object with respect to the 2D aperture plays a significant role in the ability to discern specific details of the object.

Additionally, a slight variation in the scissors' silhouette can be observed in the range dimension between the two 3D images. The backprojected image exhibits a slightly rounded shape, while the DBS image displays a minor conical form. This conical shape arises from the individual dechirp factor assigned to each range bin. If a uniform dechirp factor were employed for all ranges, the silhouette would be straight in the range direction.

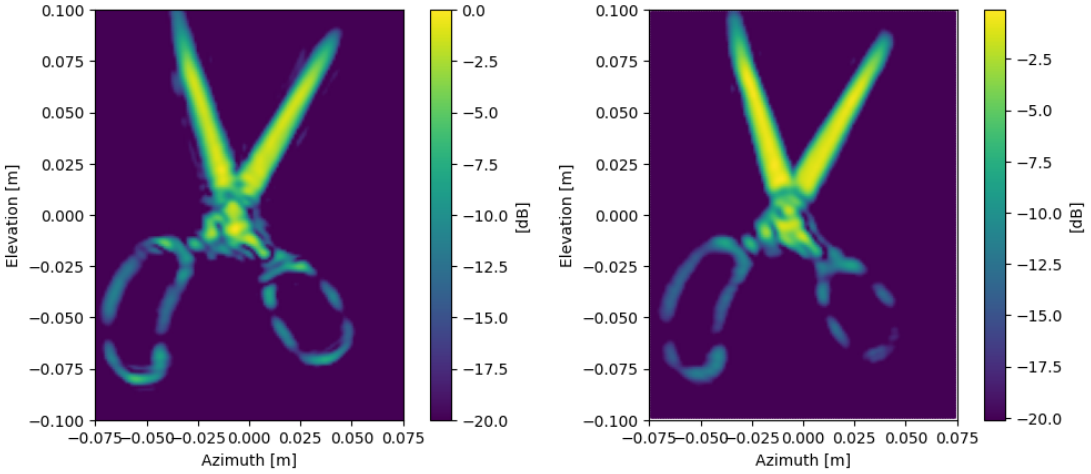

(a) Backprojection (slice at 0.2575 m)

(b) DBS (slice at 0.2627 m)

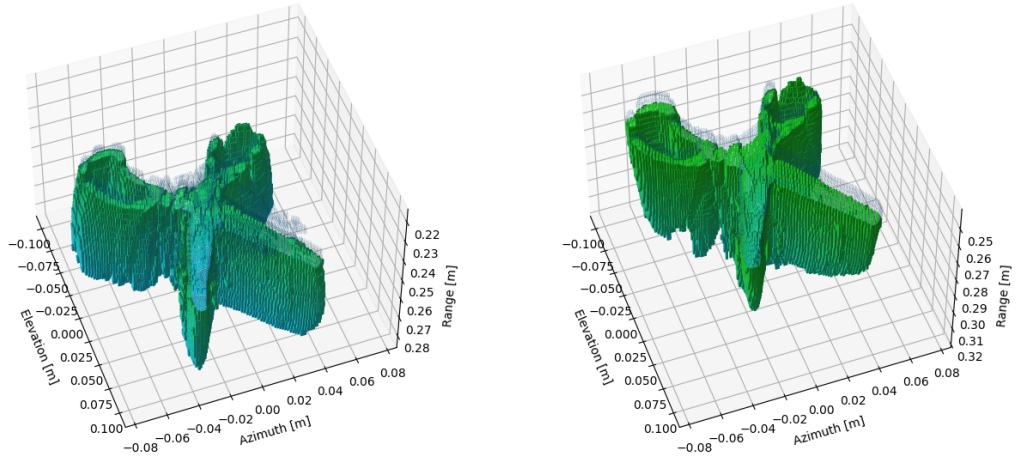

(c) Backprojection (3D representation)

(d) DBS (3D representation)

Figure 5.9: Shows the 2- and 3-dimensional images of the scissors located at a distance of approx. 0.25 m from the sensor. The 2D image is the slice of the 3D image with the highest variance.

In Figure 5.10, similar images to those in Figure 5.9 are presented, but with the scissors positioned at a distance of approximately 0.12 m from the sensor. The first noticeable distinction between the images in Figure 5.10 and Figure 5.9 is the enhanced sharpness evident in the images of Figure 5.10. This increased sharpness is a consequence of a higher SNR. Since no changes have been made to the sensor parameters between the two measurements, apart from adjusting the start point, an object closer to the sensor will exhibit a higher SNR. Consequently, the resulting image will appear sharper.

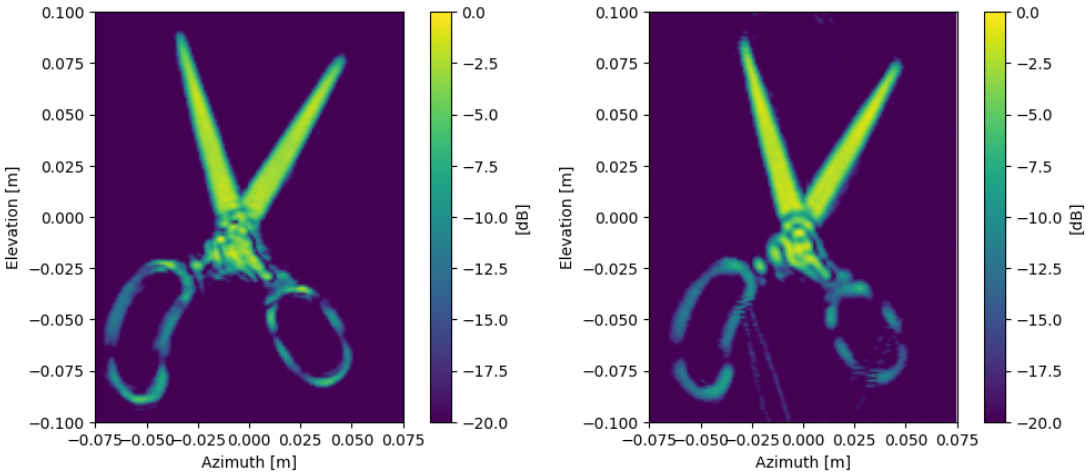

(a) Backprojection

(b) DBS

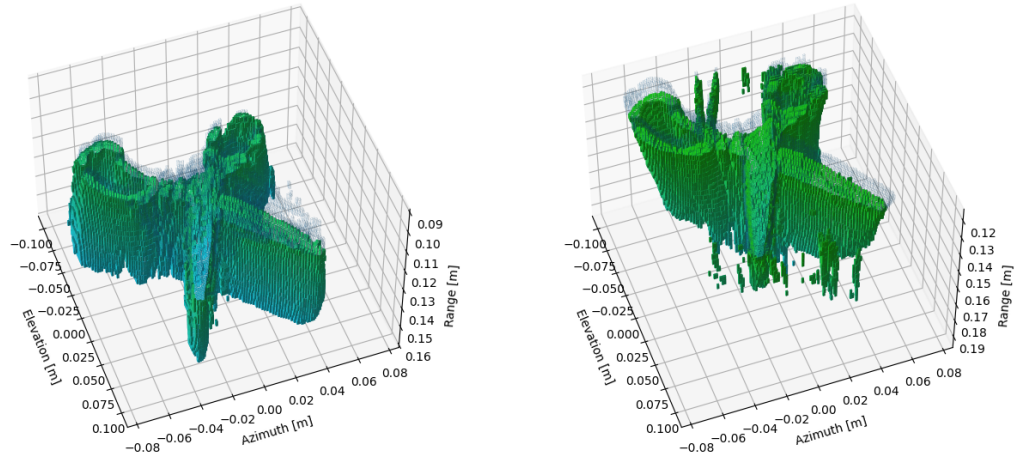

(c) Backprojection (3D representation)

(d) DBS (3D representation)

Figure 5.10: Shows the 2- and 3-dimensional images of the scissor located at a distance of approx. 0.12 m from the sensor. The 2D image is the slice of the 3D image with the highest variance.

The second noticeable difference are the artifacts which have manifested in the DBS images. These artifacts are more discernible in the 3D image, as lines protruding from the handles. They can also be seen as faint lines in the 2D rendering. These artifacts are a result of range migration. As demonstrated in the simulations depicted in Figure 4.4c, range migration artifacts manifest as sidelobes spread across multiple range bins, which is consistent with the current case. The orientation of the lines also provides insight into the dimension in which range migration is occurring. If the lines were parallel to the

elevation axis, it would indicate range migration in the elevation dimension. The same principle applies to the azimuth dimension. Since the lines are slightly diagonal and not parallel with either axis, range migration is apparent in both dimensions, however with greater extent pf migration in the elevation dimension. This corresponds with the theory considering the larger half-power beam width in the elevation dimension compared to the azimuth dimension.

Given that both setups employing the scissors (0.12 m and 0.25 m) are situated in the near-field, it might be expected that range migration in the DBS images would be more pronounced. However, the reason the DBS algorithm still performs adequately is likely attributed to the narrow half-power beam width. As demonstrated in the simulations, range migration between range bins is minimal when the beam width is narrow.

To minimize data collection time, it is crucial to sample the aperture as sparsely as possible, while maintaining image quality. In the previous images, the aperture was sampled at a spacing of 1.25 mm ($\sim \lambda/4$) in both the elevation and azimuth directions. However, recall Equation 2.19, which stated that a sampling distance at every $\lambda/4$ was exaggerated in most situations. Instead a more sparse sampling distance could be calculated by the wavelength and half-power beam width. Although this calculation assumes a a far-field scenario one can get an approximate comprehension of the sampling distance in each direction. According to Equation 2.19, the elevation direction of the aperture should be sampled at least every 3.5 mm, while the azimuth direction should be sampled every 4.9 mm.

Figure 5.11 depicts the same 2D images as in Figure 5.9, where the scissor was positioned at a distance of 0.25 m. The data remains unchanged, except for the intentional removal of some samples to simulate a coarser step length.

With a step length of 2.5 mm, neither of the algorithms exhibit signs of aliasing in the image (see Figures 5.11a and 5.11d). However, at a step length of 3.75 mm, which, according to the sampling requirements, would lead to aliasing in the elevation dimension, both algorithms display artifacts indicative of aliasing (see Figures 5.11b and 5.11e). While the backprojection image exhibits only slight artifacts around the top of the scissor blades, the DBS image reveals artifacts around the handles as well. Additionally, the extent of the DBS image is affected by a coarser sampling along the aperture. Since the algorithm is FFT based, the extent of the image depends on the highest frequency in the FFT, which is half of the sampling frequency. When the sampling becomes more sparse, the FFT extent becomes restricted as is shown by the white bars at the edges of the DBS image.

With a steplength of 5 mm, aliasing should occur in both dimensions. As is apparent in Figures 5.11c and 5.11f, where both images show multiple scissor silhouettes overlapped on top of the first one. Additionally, this shows that even if Equation 2.19 is based on a far-field approximation the same expression can be used in near-field scenarios as a good indicator of the maximum allowed sampling distance along the aperture to avoid aliasing.

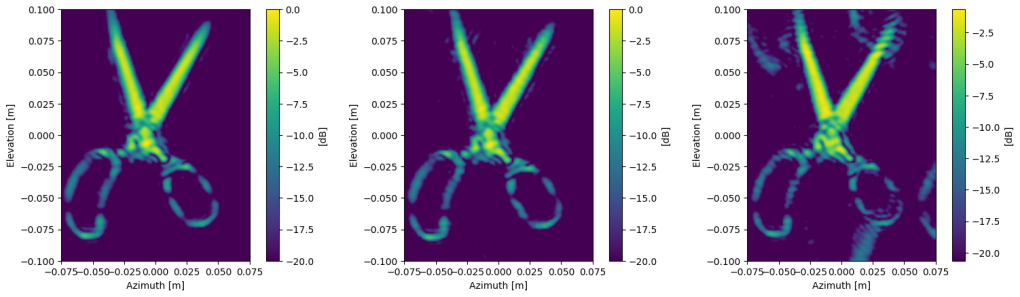

(a) BP, steplength: 2.5 mm ($\sim \lambda/2$)

(b) BP, steplength: 3.75 mm ($\sim 3\lambda/4$)

(c) BP, steplength: 5 mm ($\sim \lambda$)

(d) DBS, steplength: 2.5 mm ($\sim \lambda/2$)

(e) DBS, steplength: 3.75 mm ($\sim 3\lambda/4$)

(f) DBS, steplength: 5 mm ($\sim \lambda$)

Figure 5.11: Shows the scissor on a distance of 0.25 from the sensor with different steplengths along the 2-dimensional aperture. The images with caption "BP" are generated using the back-projection algorithm.

Chapter 6

Discussion and Conclusion

This thesis has described the fundamental theory of SAR and illustrated this theory through simulations and measurements using Acconeer's mmWave pulsed coherent radar system. This chapter will discuss and summarize the results and conclusions presented in previous chapters in accordance with the objectives stated in the introduction in Chapter 1. It will also conclude with a description of the limitations and challenges of the simulations and measurements in this thesis to suggest areas of improvement and further work.

6.1 Summary

In Chapter 1, a list of objectives was presented, creating the framework of the thesis. The first item concerned the description of the fundamental SAR concepts applying a PCR perspective. This was achieved in both the overview in Chapter 2 and the theory in Chapter 3, where it was demonstrated how the frequency concepts could be transformed into considering already range-compressed data as in PCR.

The second objective referred to showcasing the possibilities of near-field SAR with relatively simple algorithms. This was the purpose of Chapter 5, where both a one-dimensional and two-dimensional aperture were utilized to demonstrate the achievable resolution and quality of the generated images. The objects in the images were clearly distinguishable for both aperture setups; however, adding an additional dimension to the aperture resulted in a clearly increased ability to accomplish even more detailed images. Nonetheless, the restricted resolution in the range direction persisted since it depends on the pulse length.

The third objective regarded a demonstration and analysis of the advantages and disadvantages between the frequency- and time-based algorithms. The focus of the analysis was to compare the basic frequency-based algorithm, Doppler Beam Sharpening, with the time-based algorithm, Global Backprojection, to emphasize the difference between

the two approaches in real scenarios and demonstrate how they perform in the near-field. Although the algorithms operate in radically different ways, the difference between the final images, assuming a sufficiently high sampling rate and suitable conditions, was not very distinct. However, it should be noted that the phrase "suitable conditions" is key to obtaining good SAR images.

As shown by the simulations, the change in beam width and aperture length compared to the distance to the scatterer had a significant impact on the DBS image but not on the backprojected image. The measurements also revealed that the DBS image started to exhibit artifacts when the target was placed in close proximity to the sensor. However, before these changes occurred, the images from the two algorithms were highly similar, with the advantage of DBS requiring substantially fewer computations. The reason for the similarity in results between the two algorithms is the highly controlled environment where each sampling position could be precisely determined and errors and noise minimized, creating optimal conditions for all SAR algorithms. While this setup may differ from non-laboratory conditions, it effectively showcases the potential of both algorithms when favorable conditions are present. By combining these findings with the simulation results that incorporated errors and noise, a good understanding of each algorithm's capabilities under specific circumstances can be gained, achieving the final objective of the thesis.

6.2 Further Work

The challenge of near-field SAR lies in selecting the suitable algorithm for a given use case. Many cases, such as obstacle detection, object identification, and medical imaging, where the possibility of applying near-field SAR is currently explored, often encounter less controlled environments comprared to the lab setting. Instead, these scenarios face challenges of non-linear and non-uniform sampled collection paths, fast processing requirements, and the demand for fast collection times. Consequently, these challenges identify several areas for improvement and provide interesting opportunities for further work.

For the scenario of a non-linear collection path with non-uniform sampling, the backprojection algorithm remains viable. However, to shorten the processing time, it would be desirable to apply a frequency-based algorithm. It would therefore be interesting to explore the use of the non-uniform discrete Fourier transform in the algorithms for such scenarios. Another interesting aspect would be to divide the non-linear collection path into small, approximately linear portions to create several images and explore different possibilities of combining the images into a larger and more detailed image.

Another area for improvement is the collection time. The process of data collection for the 3D images shown in Chapter 5 required approximately 40 minutes since the sensor had to be moved to every measuring position. For concealed weapons detection and medical imaging, where the subject often is a human, a short collection time is of utmost

importance to minimize movement during the measurement. One could therefore explore the option of using an array of sensors to create the image, either by joining the images after processing or joining the data before processing.

Finally, a third aspect that could be interesting to examine is the use of neural networks together with SAR images for object identification in situations where either the object is concealed or a camera is too costly. Many pre-trained image classifier networks already exist, but one could explore their effectiveness on SAR images.

Chapter 7

Bibliography

[1] K. Raney, *Radars*, pp. 547–558. New York, NY: Springer New York, 2014.

[2] J. van Zyl, *Data Processing, SAR Sensors*, pp. 136–140. New York, NY: Springer New York, 2014.

[3] R. L. Giorgio Franceschetti, *Synthetic Aperture Radar Processing*. CRC Press LLC, 1999.

[4] K. Raney, *Radar, Synthetic Aperture*, pp. 536–547. New York, NY: Springer New York, 2014.

[5] W. A. H. Mark A. Richards, James A. Scheer, *Principles of modern radar Volume I Basic principles*. SciTech Publishing, Inc., 2010.

[6] Acconeer, *Hardware and Physical Integration Guideline PCR Sensors A111 & A121*, March 2023. User Guide.

[7] H.-J. Li and Y.-W. Kiang, "10 - radar and inverse scattering," in *The Electrical Engineering Handbook* (W.-K. CHEN, ed.), pp. 671–690, Burlington: Academic Press, 2005.

[8] C. Wolff and K. Hoel, "Maximum unambiguous range." `https://www.radartutorial.eu/01.basics/Maximum%20Unambiguous%20Range.en.html`, 2023. Accessed on June 19, 2023.

[9] D. Sheen, D. McMakin, and T. Hall, "Three-dimensional millimeter-wave imaging for concealed weapon detection," *IEEE Transactions on Microwave Theory and Techniques*, vol. 49, no. 9, pp. 1581–1592, 2001.

[10] M. E. Yanik and M. Torlak, "Near-field 2-d sar imaging by millimeter-wave radar for concealed item detection," in *2019 IEEE Radio and Wireless Symposium (RWS)*, pp. 1–4, 2019.

[11] Y. Gao and R. Zoughi, "Millimeter wave reflectometry and imaging for noninvasive diagnosis of skin burn injuries," *IEEE Transactions on Instrumentation and Measurement*, vol. 66, no. 1, pp. 77–84, 2017.

[12] K. T. Selvan and R. Janaswamy, "Fraunhofer and fresnel distances: Unified derivation for aperture antennas," *IEEE Antennas and Propagation Magazine*, vol. 59, no. 4, pp. 12–15, 2017.

[13] A. AB, "Fom: Figures of merit." `https://docs.acconeer.com/en/latest/handbook/a121/in_depth_topics/fom.html?highlight=resolution#radial-resolution`, 2023. Accessed on June 19, 2023.

[14] R. M. Petre Stoica, *Spectral Analysis of Signals*. Prentice Hall, Inc, 2005.

[15] I. Cumming and J. Bennett, "Digital processing of seasat sar data," in *ICASSP '79. IEEE International Conference on Acoustics, Speech, and Signal Processing*, vol. 4, pp. 710–718, 1979.

[16] C. Cafforio, C. Prati, and F. Rocca, "Sar data focusing using seismic migration techniques," *IEEE Transactions on Aerospace and Electronic Systems*, vol. 27, no. 2, pp. 194–207, 1991.

[17] A. Yegulalp, "Fast backprojection algorithm for synthetic aperture radar," in *Proceedings of the 1999 IEEE Radar Conference. Radar into the Next Millennium (Cat. No.99CH36249)*, pp. 60–65, 1999.

[18] L. Ulander, H. Hellsten, and G. Stenstrom, "Synthetic-aperture radar processing using fast factorized back-projection," *IEEE Transactions on Aerospace and Electronic Systems*, vol. 39, no. 3, pp. 760–776, 2003.

[19] M. I. Duersch and D. G. Long, "Analysis of time-domain back-projection for stripmap sar," *International Journal of Remote Sensing*, vol. 36, no. 8, pp. 2010–2036, 2015.

[20] E. C. Zaugg and D. G. Long, "Generalized frequency scaling and backprojection for lfm-cw sar processing," *IEEE Transactions on Geoscience and Remote Sensing*, vol. 53, no. 7, pp. 3600–3614, 2015.

[21] J. Lopez-Sanchez and J. Fortuny-Guasch, "3-d radar imaging using range migration techniques," *IEEE Transactions on Antennas and Propagation*, vol. 48, no. 5, pp. 728–737, 2000.

[22] Z. Wang, Q. Guo, X. Tian, T. Chang, and H.-L. Cui, "Near-field 3-d millimeter-wave imaging using mimo rma with range compensation," *IEEE Transactions on Microwave Theory and Techniques*, vol. 67, no. 3, pp. 1157–1166, 2019.

[23] S. Zhang, Y. Liu, and X. Li, "Fast entropy minimization based autofocusing technique for isar imaging," *IEEE Transactions on Signal Processing*, vol. 63, no. 13, pp. 3425–3434, 2015.

[24] Acconeer, “A121 Radar Sensor,” 2022.